International Journal of Heat and Fluid Flow 121 (2026) 110631

Contents lists available at ScienceDirect

International Journal of Heat and Fluid Flow

journal homepage: www.elsevier.com/locate/ijhff

A modified Reynolds analogy for the Gyroid TPMS in laminar flow: Thermal-hydraulic correlations, numerical validation and multi-objective optimisation ☆

L. Savoldi [a],*, A. Cammi [b,c], E. Gajetti [a], L. Marocco [c]

[a] MAHTEP Group, Dipartimento Energia, Politecnico di Torino, Italy
[b] Department of Mechanical & Nuclear Engineering, Khalifa University, and Emirates Nuclear Technology Center (ENTC), Abu Dhabi, United Arab Emirates
[c] Dipartimento di Energia, Politecnico di Milano, Milano, Italy

ARTICLE INFO

Keywords:
TPMS
Gyroid
Reynolds analogy
Heat transfer
Friction factor
Optimisation
Laminar flow

ABSTRACT

Triply Periodic Minimal Surfaces (TPMS) are increasingly adopted as heat-transfer structures thanks to their smooth curvature, tunable porosity and high surface-to-volume ratio. In the present work, we focus on the Gyroid topology in laminar flow ($20 \leq Re \leq 100$) and develop a modified Reynolds analogy linking thermal and hydraulic behaviour through compact engineering correlations. Using CFD datasets obtained under both prescribed wall temperature and imposed wall heat-flux boundary conditions, we analyse the friction factor, Nusselt number and Stanton number over the porosity range $0.3 \leq \varphi \leq 0.7$. A Darcy–Forchheimer interpretation of the hydraulic behaviour shows that the investigated operating window spans the transition from a predominantly Darcian regime to a mixed viscous–inertial regime while remaining entirely laminar. Three alternative forms of modified Reynolds analogy are calibrated, yielding correlations that reproduce the CFD data with residual deviations of 10%–15%. The resulting correlations are then employed for reduced-order thermo–hydraulic optimisation based on heat-transfer enhancement and pumping-power minimisation. Among the three formulations, only the correlation including a porosity-dependent Reynolds-number correction generates an internal Pareto front, highlighting the role of inertial transport in determining the optimal thermo–hydraulic trade-off. The proposed framework enables the prediction of thermal performance directly from hydraulic information and provides a reduced-order design tool for Gyroid-based heat-transfer applications.

1. Introduction

Triply Periodic Minimal Surfaces (TPMS) are increasingly used as architected cores in compact heat exchangers and heat sinks, thanks to their smooth curvature, high surface-to-volume ratio and the possibility of tuning porosity and wall thickness over a wide range (Dutkowski et al., 2022; Yeranee and Rao, 2022; Gado et al., 2024). The advent of metal additive manufacturing has made these geometries practically realisable for thermal management applications, and a growing body of work now documents their structural and thermo–hydraulic performance (Savoldi et al., 2026). Among the various TPMS topologies, the Gyroid has emerged as one of the most promising candidates, combining good mechanical stiffness with favourable flow and heat transfer characteristics (Yeranee and Rao, 2022; Savoldi et al., 2026; Padrão et al., 2024; Brambati et al., 2024). Recent numerical and experimental studies have proposed correlations for Nusselt number and friction factor in Gyroid and other TPMS-based heat exchangers, relating Nu and f to Reynolds number Re, porosity φ and additional geometric parameters (Padrão et al., 2024; Brambati et al., 2024). However, in almost all cases the hydraulic and thermal behaviours are treated separately: a friction-factor (or pressure-drop) correlation is fitted independently from a heat-transfer correlation, and design must rely on both, or on repeated CFD simulations, whenever topology or porosity change.

From a theoretical point of view, the similarity between momentum and heat transfer has long been formalised through Reynolds-type analogies.

In its original formulation, the Reynolds analogy was derived for fully developed turbulent flow over smooth walls, with negligible pressure loss (shape drag) and Prandtl number Pr close to unity. Under these assumptions, the governing equations for momentum and energy exhibit similar structure, leading to a proportionality between skin-friction coefficient C_f and Stanton St number, commonly expressed

☆ This article is part of a Special issue entitled: 'THMT-11 Special Issue' published in International Journal of Heat and Fluid Flow.

* Corresponding author.
E-mail address: laura.savoldi@polito.it (L. Savoldi).

https://doi.org/10.1016/j.ijheatfluidflow.2026.110631
Received 14 February 2026; Received in revised form 10 August 2026; Accepted 15 August 2026
Available online 31 August 2026

Nomenclature

English symbols

A_i	Cross-sectional fluid area at streamwise station i
A_{wet}	Wetted solid–fluid interfacial area
c_p	Specific heat capacity at constant pressure
C_f	Skin-friction coefficient based on area-averaged wall shear stress
C_F	Forchheimer inertial coefficient
D_h	Hydraulic diameter, $4V_{\text{fluid}}/A_{\text{wet}}$
$D_{h,\text{rel}}$	Relative hydraulic diameter, D_h/L
f	Pressure-drop Darcy friction factor
Fh	Forchheimer number, ratio of inertial to viscous Darcy–Forchheimer losses
h	Area-averaged convective heat-transfer coefficient
j	Chilton–Colburn heat-transfer factor
k	Thermal conductivity
K	Permeability
K_{rel}	Relative permeability, K/L^2
L	Cubic unit-cell length
$\dot{m}$	Mass flow rate
$\dot{V}$	Volumetric flow rate
Nu	Nusselt number based on D_h
Nu_K	Permeability-based Nusselt number, $h\sqrt{K}/k$
p	Pressure
P_K	Permeability-based hydraulic-cost index
P_{pump}	Pumping-power index
Pr	Prandtl number, ν/α
q_w	Wall heat flux
Re_{D_h}	Reynolds number based on U_b and D_h
Re_K	Reynolds number based on U_s and $\sqrt{K}$
St	Stanton number, $Nu/(Re\,Pr)$
t	Gyroid isovalue controlling porosity
T	Temperature
T_b	Bulk or mass-flow-averaged temperature
T_w	Wall temperature
U_b	Pore or intrinsic bulk velocity, U_s/φ
U_s	Superficial or Darcian velocity, $\dot{V}/L^2$
V_{cell}	Unit-cell volume
V_{fluid}	Fluid volume in the unit cell

Greek symbols

α	Thermal diffusivity, $k/(\rho c_p)$
Δh	Characteristic mesh size
Δp	Pressure drop across one periodic cell
ΔT_{lm}	Logarithmic mean temperature difference
ΔT_{o-i}	Bulk temperature rise between outlet and inlet
γ	Observed order of grid convergence
μ	Dynamic viscosity
ν	Kinematic viscosity, μ/ρ
ρ	Fluid density
τ_w	Local wall shear stress
$\overline{\tau}_w$	Surface-averaged wall shear stress
φ	Porosity or fluid volume fraction
ψ	Generic monitored quantity in the grid-convergence analysis
θ	Normalised temperature used for thermal periodicity

Abbreviation

AFM	Atomic force microscopy
CFD	Computational fluid dynamics
GCI	Grid Convergence Index
IWP	I-graph and wrapped package TPMS topology
LMTD	Logarithmic mean temperature difference
MAPE	Mean absolute percentage error
PCM	Phase-change material
RMSE	Root mean square error
TPMS	Triply Periodic Minimal Surface

Subscripts, superscripts and operators

b	Bulk or pore-averaged quantity
$cell$	Unit-cell quantity
CFD	Quantity obtained from CFD simulations
$corr$	Quantity obtained from the analytical correlation
D_h	Quantity based on the hydraulic diameter
f	Fluid phase or friction-related quantity, depending on context
h	Hydraulic-diameter-related quantity
i	Streamwise station or mesh index
K	Quantity based on permeability
lm	Logarithmic mean value
$o-i$	Outlet-minus-inlet difference
$pump$	Pumping-power-related quantity
rel	Relative or dimensionless quantity
s	Superficial or Darcian quantity
w	Wall quantity
$\overline{(\cdot)}$	Surface- or area-averaged quantity
$\dot{(\cdot)}$	Time rate or flow-rate quantity

as

$$\frac{C_f}{2} \approx St = \frac{Nu}{Re\,Pr}$$

which is sometimes recast in terms of the Reynolds-analogy factor $2St/C_f \approx 1$ (Incropera et al., 2011; Bergman et al., 2011).

If, in its original form, the analogy is expressed in terms of the skin-friction coefficient C_f, which is directly related to the wall shear stress, in practical engineering applications, the analogy is commonly reformulated in terms of the friction factor f. This reformulation replaces the local shear-based description with a global, pressure-drop-based quantity that is directly accessible in experiments and robust in complex geometries. The Chilton–Colburn j-factor formulation extends this concept to fluids with $Pr \neq 1$:

$$j = \frac{Nu}{Re\,Pr^{1/3}}$$

providing a convenient framework for comparing momentum and heat transfer. The relationship between j and the friction factor, often referred to as the "modified Reynolds analogy", has become a standard correlation framework in turbulent internal flows and boundary layer flows (Chilton and Colburn, 1934; Cengel and Ghajar, 2014), and the "area goodness factor" j/f is often used as a key performance indicator to compare the combined thermal and hydraulic performance of different cooling configurations. Although originally developed for turbulent flows, Reynolds-type analogies have subsequently been extended to laminar flows and other complex transport regimes, demonstrating that departures from the classical analogy arise whenever momentum and heat transfer are governed by different physical mechanisms (Mahulikar and Herwig, 2008; Fukagata et al., 2002; Zhang et al., 2014; Sucec, 2020; Forooghi et al., 2021; Secchi et al., 2025).

Porous media and packed beds constitute an important class of geometrically complex systems in which the possibility of inferring heat-transfer behaviour from pressure-drop data through analogy-type arguments is particularly appealing. Recent studies on packed beds and granular flows have demonstrated that Reynolds-type analogies can be constructed at a macroscopic level, although classical relations such as $f/2 \sim St$ generally fail due to strong pressure-drag effects (Park et al., 2024; Wu and Hibiki, 2025). In particular, Park et al. (2024) showed experimentally that the discrepancy between hydraulic and thermal transport in packed beds originates from pressure-drag contributions that have no direct thermal counterpart, highlighting the need for modified Reynolds analogies in such complex geometries. However, in these porous systems the analogies are generally carried out qualitatively in terms of area goodness factor, and explicit correlations of the type

$$St = \Phi(f, Re)$$

are not sought.

For regular lattices based on TPMS, several studies have documented how porosity, cell size and topology affect pressure drop and Nusselt number in Gyroid and related TPMS structures, in both laminar and turbulent regimes (Dutkowski et al., 2022; Yeranee and Rao, 2022; Padrão et al., 2024; Brambati et al., 2024), proposing independent correlations for Nu and f (Khalil et al., 2022; Iyer et al., 2022; Yan et al., 2024).

Some works adopt Chilton–Colburn-type performance parameters (e.g. j-factor or area goodness factor) to compare TPMS with conventional geometries and other lattices (Zhang et al., 2025). Recent investigations have further explored TPMS structures through parametric optimisation, advanced cooling concepts, porous-medium formulations and pore-scale multi-objective optimisation (Samson et al., 2023; Saxena et al., 2025; Men et al., 2025; Carpenter and Jin, 2024). Despite these developments, hydraulic and thermal behaviours are still almost invariably treated separately, requiring either independent pressure-drop and heat-transfer correlations or dedicated thermal simulations. Consequently, a topology-specific Reynolds analogy capable of predicting heat-transfer behaviour directly from hydraulic information is still lacking. A first step in this direction was presented by the present authors in Savoldi et al. (2025), where a modified Reynolds analogy was investigated for Gyroid in laminar regime. That study formulated correlations of the form

$$Nu = \Phi(\varphi, C_f, Re)$$

and demonstrated that, for TPMS at unit Prandtl number, the Nusselt number can be related to skin-friction coefficient and porosity with a standard deviation of 10–15%. The analysis, limited to a narrower porosity range, formulated a first explicit correlation of Nu with the friction factor, but did not exploit the analogy for optimisation purposes. Furthermore, although Darcy–Forchheimer formulations are routinely employed to describe the hydraulic behaviour of TPMS and porous media, their connection with Reynolds-analogy concepts in the framework of porous media has not yet been investigated. Establishing such a connection could provide a physical interpretation of the thermo–hydraulic coupling and enable reduced-order prediction and optimisation tools based solely on hydraulic information.

In geometrically complex systems such as TPMS, the skin-friction coefficient C_f, which is directly linked to the area-averaged wall shear stress and therefore represents the most fundamental quantity from a theoretical standpoint, is difficult to access experimentally. On the other hand, in fully three-dimensional CFD simulations it is sensitive to mesh resolution and numerical noise. By contrast, the friction factor f is a global quantity obtained directly from pressure-drop measurements or from CFD simulations with periodic boundary conditions. Unlike C_f, the friction factor naturally incorporates both viscous and form-drag contributions and can be robustly evaluated even in complex porous geometries. For this reason, the present work deliberately focuses on the reformulation of the Reynolds analogy in terms of the friction factor rather than the skin-friction coefficient. This choice is also consistent with recent studies on packed beds and porous media, where pressure-drop-based quantities provide a more practical description of thermo–hydraulic behaviour than wall-shear-based metrics (Park et al., 2024).

The present study addresses the question of whether the thermal behaviour of a Gyroid TPMS, selected as the representative topology because of its widespread use in heat-transfer applications, can be reconstructed directly from hydraulic information through a modified Reynolds analogy. The analysis is restricted to the solid Gyroid topology in laminar incompressible flow at unit Prandtl number, $20 \leq Re \leq 100$ and $0.3 \leq \varphi \leq 0.7$. The selected porosity range is representative of practically relevant solid-network TPMS structures. Porosities significantly below 0.3 lead to extremely narrow flow passages and increased manufacturing complexity, whereas porosities substantially above 0.7 generate very thin solid walls with reduced structural robustness. Moreover, porosities close to 50% are also relevant for sheet-based TPMS architectures, where the two complementary fluid domains obviously exhibit effective porosities below 50%. The investigated interval therefore encompasses a large fraction of the practically relevant design space for both solid and sheet TPMS structures.

The objective of the present work is to establish a reduced-order thermo–hydraulic framework capable of predicting heat-transfer performance directly from hydraulic quantities. To achieve this goal, a hydraulic correlation for the friction factor is first developed and interpreted within a Darcy–Forchheimer framework. Modified Reynolds analogies relating Stanton number and friction factor are then formulated and assessed using CFD data obtained under different thermal boundary conditions. Finally, the resulting correlations are employed within a reduced-order thermo–hydraulic optimisation framework to identify optimal trade-offs between heat-transfer enhancement and pumping-power consumption.

2. Methodology: CFD configuration and post-processing

2.1. Computational setup

The CFD simulations used in this study were performed on a single solid Gyroid unit cell with fully periodic hydraulic and thermal boundary conditions, see Fig. 1, assumed to be representative of an infinitely repeated periodic medium. This approach allows the hydraulic and thermal behaviour of the TPMS to be investigated under fully developed conditions while minimising the computational cost. Consequently, effects associated with finite-size geometries, entrance regions, outlet conditions and external walls are not captured. These phenomena may influence the performance of practical heat exchangers and heat sinks, but periodic-cell simulations remain a widely accepted methodology for extracting geometry-specific transport properties and reduced-order correlations for porous and TPMS structures.

The Gyroid surface is implicitly defined by the trigonometric function:

$$\sin\left(\frac{2\pi x}{L}\right)\cos\left(\frac{2\pi y}{L}\right)+\sin\left(\frac{2\pi y}{L}\right)\cos\left(\frac{2\pi z}{L}\right)+\sin\left(\frac{2\pi z}{L}\right)\cos\left(\frac{2\pi x}{L}\right)=t \tag{1}$$

where L is the unit cell size and t is the isovalue parameter that controls the porosity φ through the volume fraction of the level-set region. Specifically, the fluid domain corresponds to the region where $G(\mathbf{x}) < t$ (or $> t$ depending on convention), and the solid phase occupies the complementary region. The domain was generated using nTop software (nTop, 2026), whereas the simulations were performed using the OpenFOAM software (ESI OpenCFD, 2026).

Laminar flow conditions are ensured everywhere in the fluid domain, so that the set of conservation laws that are solved is:

$$\frac{\partial \rho}{\partial t} + \nabla \cdot (\rho \mathbf{v}) = 0 \tag{2}$$

$$\frac{\partial (\rho \mathbf{v})}{\partial t} + \nabla \cdot (\rho \mathbf{v} \otimes \mathbf{v}) = -\nabla \cdot (p\mathbf{I}) + \nabla \cdot \mathbf{T} \tag{3}$$

$$\frac{\partial (\rho E)}{\partial t} + \nabla \cdot (\rho E \mathbf{v}) = \nabla \cdot (\mathbf{v} \cdot \boldsymbol{\sigma}) - \nabla \cdot \mathbf{q} \tag{4}$$

where ρ is the density, $\mathbf{v}$ the fluid velocity, p the pressure, $\mathbf{I}$ the identity tensor, $\mathbf{T}$ the viscous stress tensor, E the total energy per unit mass and $\mathbf{q}$ the heat flux, modelled using Fourier's law.

For the constant-property incompressible cases considered here, the governing equations can be stated more directly as

$$\nabla \cdot \mathbf{v} = 0 \tag{5}$$

$$\rho(\mathbf{v} \cdot \nabla)\mathbf{v} = -\nabla p + \mu \nabla^2 \mathbf{v} \tag{6}$$

$$\rho c_p \, \mathbf{v} \cdot \nabla T = k \nabla^2 T \tag{7}$$

with the pressure field including the imposed periodic pressure jump.

For this study the Pr number is set to unity. The choice $Pr = 1$ is consistent with the objective of the present work, namely the investigation of Reynolds-analogy concepts in TPMS structures. For $Pr \approx 1$, momentum and thermal diffusivities are comparable, resulting in hydrodynamic and thermal boundary layers of similar thickness. Under these conditions, similarities between momentum and heat-transfer mechanisms are expected to be strongest, making this regime a natural starting point for the development and assessment of modified Reynolds analogies. If this choice simplifies the physics and is appropriate to identify geometric trends, extrapolations to fluids with $Pr \neq 1$ should be done with caution (see Conclusions and future work).

2.2. Hydraulic and thermal boundary conditions

A schematic representation of the employed boundary conditions is reported in Fig. 1. Periodic boundary conditions were imposed on all external faces of the computational domain. A pressure-gradient-driven flow was enforced by prescribing a finite pressure jump between two opposite periodic faces, corresponding to the main flow direction. The remaining two pairs of periodic faces were assigned zero pressure jump, thereby enforcing periodicity without inducing any net transverse flow. The resulting volumetric flow rate was used to compute the superficial velocity and the Reynolds number, see Section 2.4. This formulation reproduces the behaviour of an infinitely long periodic medium and eliminates inlet and outlet effects that would otherwise influence the pressure losses and wall shear stresses.

Two different thermal boundary conditions were considered in order to assess the robustness of the proposed Reynolds-analogy framework. In the first configuration, a spatially uniform wall temperature was imposed over the entire Gyroid surface (*constant wall temperature*, T_w). In the second configuration, a spatially uniform heat flux was imposed over the same surface (*constant wall heat flux*, q_w). The two conditions represent the most common idealised thermal boundary conditions employed in internal-flow heat-transfer studies. The objective of the present work is not to model a specific heat-exchanger configuration, but rather to investigate the intrinsic coupling between momentum and convective heat transfer within the fluid domain of the Gyroid. For this reason, the above-mentioned idealised thermal boundary conditions were intentionally adopted. These conditions isolate fluid-side transport mechanisms and allow geometry-induced effects to be analysed independently of the thermal conductivity, thickness and material properties of the solid phase. Real applications may exhibit significant conduction within the solid structure, requiring conjugate heat-transfer simulations. Such effects are beyond the scope

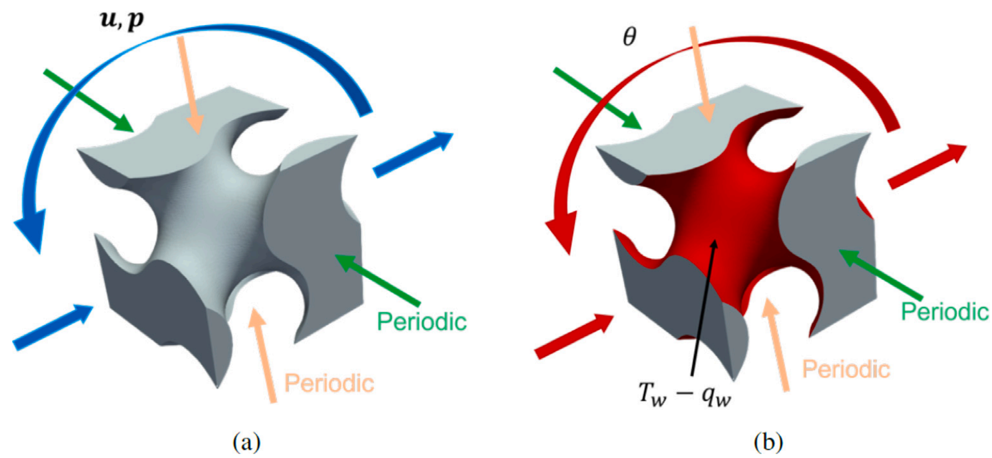

Fig. 1. Computational domain and boundary conditions adopted for the periodic Gyroid unit cell. The hydraulic problem is driven by an imposed pressure jump between periodic faces (a), while thermal periodicity is enforced by keeping the same reduced temperature θ at inlet and outlet (b). Both constant wall temperature and constant wall heat-flux boundary conditions are considered.

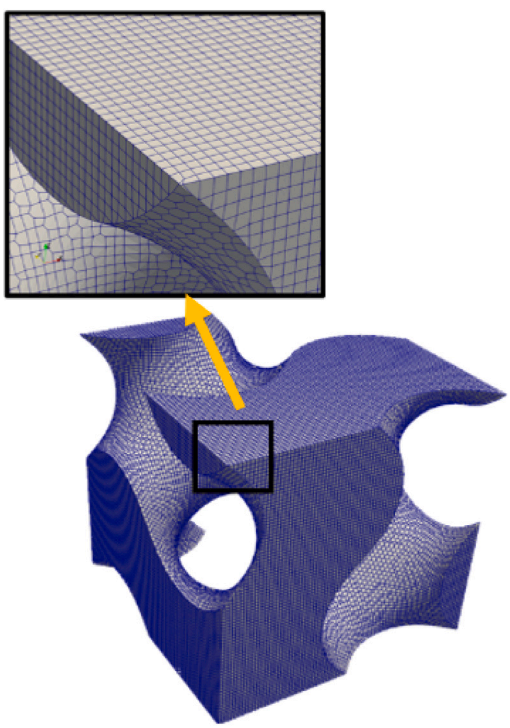

Fig. 2. Computational mesh Ref2 (1.54×10^5 cells) used for the simulation of the Gyroid cell (OpenFOAM/snappyHexMesh) with $\varphi = 0.5$. Details on solution verification are in Section 2.3.

of the present work, and represent an important direction for future investigations.

In both cases the thermal periodicity was enforced by the same reduced temperature θ on the inlet and outlet faces in the flow direction. θ is defined as:

$$\theta = \frac{T_w - T}{T_w - T_b} \tag{8}$$

and T_b is the bulk temperature, whereas T_w is the imposed wall temperature.

2.3. Grid generation and mesh convergence study (solution verification)

The computational mesh was generated using the OpenFOAM mesher `snappyHexMesh`, resulting in a predominantly hexahedral body-fitted discretisation of the Gyroid surface, see Fig. 2. Since the present investigation is restricted to laminar flow conditions ($20 \leq$ Re ≤ 100), no dedicated boundary-layer refinement was introduced.

A dedicated mesh-convergence study was carried out on the most demanding operating condition considered in the present work, corresponding to the lowest porosity $\varphi = 0.3$ and highest Reynolds number $Re = 100$. Four progressively refined meshes were generated for the Gyroid geometry, containing approximately 3.8×10^4 (Ref4), 6.5×10^4 (Ref3), 1.54×10^5 (Ref2) and 5.18×10^5 (Ref1) cells, respectively. The refinement was performed uniformly in all the directions. The characteristic mesh size was defined as

$$\Delta h = \sqrt[3]{\frac{V_f}{N_{\text{cells}}}} \tag{9}$$

where (V_f) is the fluid volume and (N_{cells}) is the total number of computational cells. Fig. 3 reports the convergence behaviour of four representative global quantities, namely the pressure drop Δp, the area-averaged wall shear stress τ_w, the area-averaged wall heat flux q_w (for constant T_w), and the bulk temperature rise ΔT_{o-i} (for constant q_w). All quantities are normalised by the value obtained with the finest mesh (Ref1). The convergence behaviour is almost monotonic for all variables.

The numerical uncertainty associated with spatial discretisation was estimated using a Grid Convergence Index (GCI) approach. The monitored quantity ψ was assumed to satisfy the asymptotic relationship

$$\psi_i - \psi_\infty = \alpha \Delta h_i^\gamma \tag{10}$$

where ψ_i is the value obtained on the ith mesh, ψ_∞ is the extrapolated solution corresponding to vanishing mesh size, Δh_i is the characteristic cell size, α is a proportionality coefficient and γ is the observed order of convergence. The parameters ψ_∞, α and γ were obtained through a least-squares fit of the results computed on the four progressively refined meshes.

The Grid Convergence Index was then evaluated as

$$GCI = \frac{1.25\, e_{32}^a}{r_{32}^\gamma - 1} \tag{11}$$

where e_{32}^a is the absolute difference between the solutions obtained on meshes Ref3 and Ref2, and r_{32} is the corresponding mesh refinement ratio. Following the recommendations of the ASME V&V standard (ASME,

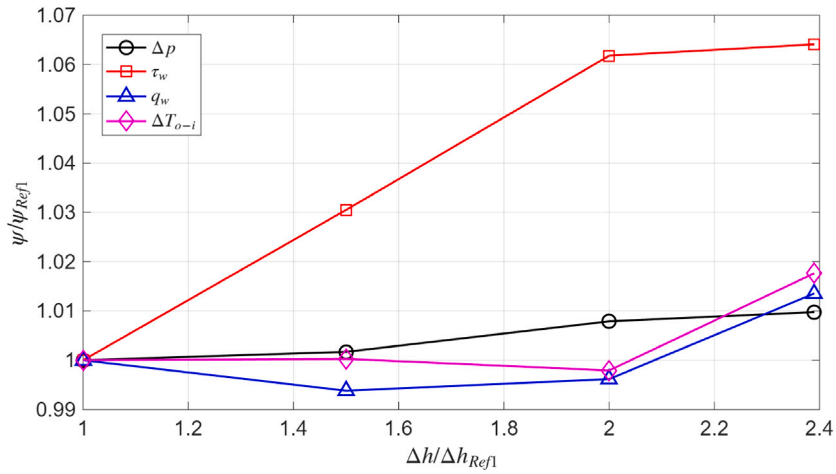

Fig. 3. Grid-convergence study for the Gyroid TPMS at ($\varphi = 0.3$) and (Re=100). The pressure drop (Δp), area-averaged wall shear stress (τ_w), area-averaged wall heat flux (q_w), and bulk temperature rise (ΔT_{o-i}) are normalised by the corresponding value obtained with the finest mesh (Ref1).

2009), the numerical uncertainty u_{num} associated with discretisation was finally estimated as

$$u_{num} = \frac{GCI}{1.15} \tag{12}$$

The pressure drop exhibits very limited sensitivity to grid refinement, with a variation below 0.2% between the selected mesh (Ref2) and the finest grid. Similarly, the wall heat flux and bulk temperature rise remain essentially unchanged, with differences smaller than 1%. The largest discretisation sensitivity is observed for the wall shear stress, which varies by approximately 3% between Ref2 and Ref1. This behaviour is expected because τ_w depends directly on near-wall velocity gradients, which are intrinsically more sensitive to local discretisation errors in highly convoluted three-dimensional geometries.

For the selected mesh (Ref2), the estimated u_{num} are approximately 1% for the pressure drop, 7% for the area-averaged wall shear stress, 0.3% for the wall heat flux and 0.2% for the bulk temperature rise. These results indicate that the adopted mesh resolution provides an appropriate compromise between numerical accuracy and computational cost.

2.4. Definition of the hydrodynamic and thermal quantities

All dimensional and non-dimensional quantities used in this work are defined here for clarity and reproducibility. The *Porosity* is defined as the ratio of fluid (channel) volume to total cell volume:

$$\varphi = \frac{V_{\text{fluid}}}{V_{\text{cell}}} \tag{13}$$

where $V_{\text{cell}} = L^3$ is the volume of the cubic unit cell. This quantity is also referred to as void fraction or channel volume fraction in TPMS literature.

The *pore velocity* U_b is calculated as the superficial velocity U_s divided by the porosity:

$$U_b = U_s/\varphi \tag{14}$$

The superficial (or Darcian) velocity U_s is in turn defined as the volume flow rate $\dot{V}$ divided by the total cross sectional area of the unit cell:

$$U_s = \frac{\dot{V}}{L^2} \tag{15}$$

The *hydraulic diameter* D_h is obtained from the wetted area A_{wet}, i.e. the solid-fluid interface area, per unit volume:

$$D_h = \frac{4V_{\text{fluid}}}{A_{\text{wet}}} \tag{16}$$

This definition reduces to the standard $D_h = 4A_{\text{cross}}/P_{\text{wet}}$ for simple ducts and is consistent with porous-media theory.

The Reynolds number employed throughout the present work is based on the hydraulic diameter and pore velocity:

$$Re_{D_h} = \frac{\rho U_b D_h}{\mu} \tag{17}$$

This convention ensures that Re reflects the actual velocity experienced within the pore channels and remains consistent with the heat-transfer literature on TPMS and porous structures.

The *skin friction coefficient* is defined as

$$C_f = \frac{2\overline{\tau}_w}{\rho U_b^2} \tag{18}$$

where $\overline{\tau}_w$ is the wetted-surface average shear stress. C_f represents the purely viscous contribution to drag and is the term appearing in the classical Reynolds analogy. However, C_f is difficult to measure experimentally and is more sensitive to local mesh resolution.

The Darcy *friction factor* f is defined as

$$f = \frac{\Delta p D_h}{\frac{1}{2}\rho U_b^2 L} \tag{19}$$

where Δp is the pressure drop across the periodic cell length L. Unlike C_f, the friction factor includes both viscous and form-drag contributions and can be readily obtained from experiments or CFD. Although less straightforward than C_f from an analogy perspective, f proves far more practical and robust for engineering correlations.

When looking at the lattice cell as a porous medium, the pressure drop can be modelled by the Darcy–Forchheimer law. Starting from the momentum balance for flow through a porous medium:

$$-\frac{dp}{dx} = \frac{\mu}{K}U_s + \frac{\rho C_F}{\sqrt{K}}U_s^2 \tag{20}$$

where K is the permeability [m^2] and C_F is the Forchheimer (inertial) coefficient [-]. The Darcy–Forchheimer equation provides a physically meaningful interpretation of the pressure losses within TPMS structures by explicitly separating viscous and inertial contributions. In addition to the conventional Reynolds number based on the hydraulic diameter, it is therefore useful to introduce a permeability-based Reynolds number,

$$Re_K = \frac{\rho U_s \sqrt{K}}{\mu} \tag{21}$$

which measures the ratio between inertial and viscous effects using the permeability length scale $\sqrt{K}$ rather than the hydraulic diameter.

A second quantity of interest is the Forchheimer number Fh,

$$Fh = C_F Re_K = \frac{\rho C_F U_s^2/\sqrt{K}}{\mu U_s/K} \quad (22)$$

which is exactly equal to the ratio between the inertial and viscous contributions appearing in the Darcy–Forchheimer equation. Unlike the conventional Reynolds number, which is based on the hydraulic diameter, the Forchheimer number directly quantifies the relative importance of inertial and viscous losses within the porous medium.

Consequently, $Fh \ll 1$ corresponds to a predominantly Darcian regime, whereas increasing values of Fh indicate a progressively stronger contribution of inertial effects. While the Reynolds number remains the primary parameter employed in the present work, the quantities Re_K and Fh provide a porous-medium interpretation of the flow physics and will be used later to discuss the transition from predominantly viscous to mixed viscous–inertial transport regimes.

Substituting the Darcy–Forchheimer expression into the definition of f, introducing the dimensionless quantities $D_{h,rel} = D_h/L$ and $K_{rel} = K/L^2$, and performing straightforward algebraic manipulations yields

$$f(\varphi, Re_{D_h}) = 2\varphi\left(\frac{D_{h,rel}^2}{K_{rel}Re_{D_h}} + \varphi, D_{h,rel}C_F\frac{1}{\sqrt{K_{rel}}}\right), \quad (23)$$

where $D_{h,rel}$ and K_{rel} are the dimensionless hydraulic diameter and relative permeability, defined by scaling D_h by the cell size and K by the square of the cell size, respectively. All three coefficients are expressed as simple power-law or rational functions of porosity, as shown in Gajetti et al. (2025).

The Darcy–Forchheimer representation for the friction factor explicitly separates the viscous ($\propto Re^{-1}$) and inertial (Reynolds-independent) contributions to the total pressure loss, which is desirable when fitting complex geometries where form drag plays a major role. Note again that fitting f rather than C_f allows direct use of pressure-drop measurements for practical applications.

The correlations for $D_{h,rel}$, K_{rel} and C_F, once inserted into Eq. (23), provide a compact expression for $f(\varphi, Re)$ over the entire range $0.3 \le \varphi \le 0.7$ and $20 \le Re \le 100$. This correlation will be verified a posteriori (see Fig. 6) and constitutes the hydraulic backbone of all subsequent Reynolds-analogy formulations and of the optimisation study.

As far as the *heat-transfer coefficient* h is concerned, its evaluation differs according to the thermal boundary condition adopted in the simulations.

In the case of imposed heat flux at the wall (q_w = const), the definition is

$$h = \frac{q_w}{T_w - \overline{T}_b} \quad (24)$$

where T_w is the surface-average value computed in the simulations and $\overline{T}_b$ is the average bulk temperature.

In a periodic domain with constant fluid properties, the bulk temperature across the fluid main flow direction is defined as

$$\overline{T}_b = \frac{1}{\dot{m}}\int_{A_i} \rho u_n T\, dA \quad (25)$$

where $\dot{m}$ is the mass flow rate and u_n the normal velocity component.

In the case of imposed temperature at the wall (T_w = const), the average heat-transfer coefficient follows from the overall energy balance across the periodic cell:

$$\overline{h} = \frac{\dot{m}c_p \Delta T_{\text{lm}}}{A_{\text{wet}}(T_w - T_b)}. \quad (26)$$

where the logarithmic mean temperature difference ΔT_{lm} is defined as

$$\Delta T_{\text{lm}} = \frac{T_{b,\text{out}} - T_{b,\text{in}}}{\ln\left[\frac{T_w - T_{b,\text{out}}}{T_w - T_{b,\text{in}}}\right]}. \quad (27)$$

The heat-transfer performance is expressed in dimensionless form through the Nusselt number,

$$Nu = \frac{\overline{h}D_h}{k}, \quad (28)$$

where $\overline{h}$ is the area-averaged convective heat-transfer coefficient and k the fluid thermal conductivity. For consistency with the conventional heat-transfer literature, the Nusselt number is defined in the present work using the hydraulic diameter as characteristic length scale. However, when the flow is interpreted within the Darcy–Forchheimer framework, an alternative permeability-based Nusselt number can also be introduced:

$$Nu_K = \frac{\overline{h}\sqrt{K}}{k} \quad (29)$$

The relationship between the two definitions is

$$Nu_K = Nu\frac{\sqrt{K}}{D_h} = Nu\frac{\sqrt{K_{rel}}}{D_{h,rel}}. \quad (30)$$

While the present Reynolds-analogy formulation and optimisation framework are developed in terms of the conventional Nusselt number Nu, the permeability-based quantity Nu_K will be employed later as an additional tool for interpreting the thermo–hydraulic behaviour of the Gyroid within a porous-medium perspective.

The Stanton number follows directly from

$$St = \frac{Nu}{Re_{D_h}Pr} = \frac{Nu}{Re_{D_h}} \quad (31)$$

since all simulations are carried out at $Pr = 1$. Note that from this point on throughout the correlation and optimisation sections, $Re \equiv Re_{D_h}$.

The hydraulic cost associated with a given operating condition is quantified through the pumping power, defined as the product of the pressure drop and the volumetric flow rate. Expressing the pressure drop in terms of the friction factor and the volumetric flow rate in terms of the Reynolds number yields the following dimensionless pumping-power index:

$$P_{\text{pump}} \propto \frac{\varphi f\, Re^3}{D_{h,\text{rel}}^4} \quad (32)$$

where $D_{h,\text{rel}} = D_h/L$ is the dimensionless hydraulic diameter. Unlike the commonly adopted $f Re^3$ scaling, Eq. (32) explicitly accounts for the variation of both porosity and hydraulic diameter across the investigated design space, thereby providing a physically consistent measure of the hydraulic power required to drive the flow.

The above definition is adopted throughout the present work because the modified Reynolds analogy is formulated in terms of the hydraulic-diameter-based Reynolds number. Nevertheless, when the flow is interpreted within the Darcy–Forchheimer framework, an alternative (dimensionless) measure of the hydraulic cost can be derived. Starting again from the physical definition of pumping power, and substituting the Darcy–Forchheimer pressure-drop relation expressed in terms of the superficial velocity, the following permeability-based hydraulic-cost index is obtained:

$$P_K \propto \frac{Re_K^2(1 + Fh)}{K_{rel}^2} \quad (33)$$

The first contribution corresponds to the viscous (Darcy) component of the pumping power, whereas the second accounts for the additional inertial losses associated with the Forchheimer term. With respect to P_{pump}, the parameter P_K offers an alternative interpretation of the hydraulic cost that is particularly useful when discussing the transport physics in terms of porous-medium quantities.

The correlation database consists of 45 CFD simulations obtained from five porosity values (ϕ = 0.3, 0.4, 0.5, 0.6 and 0.7) and nine Reynolds numbers for each porosity (≈ 20, ≈ 30, ≈ 40, ≈ 50, ≈ 60, ≈ 70, ≈ 80, ≈ 90 and ≈ 100). Each operating point was evaluated under two independent thermal boundary conditions (constant wall temperature and constant wall heat flux), resulting in 90 thermal cases. The

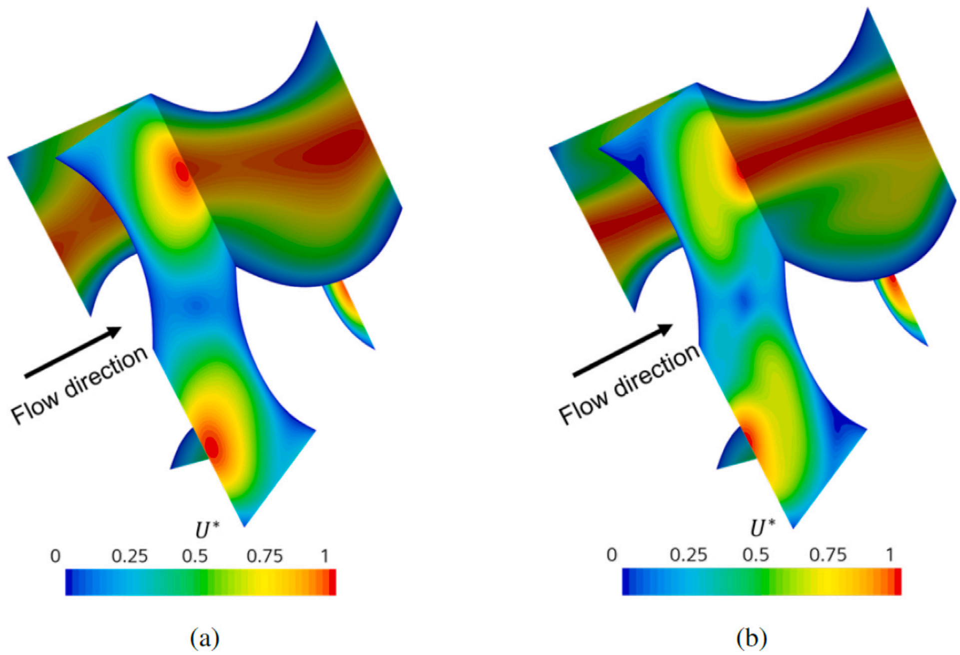

Fig. 4. Normalised velocity magnitude $U^\star = |\mathbf{u}|/U_b$ at $Re = 20$ (a) and $Re = 100$ (b).

hydrodynamic characterisation therefore comprises 45 independent operating points, whereas the regression for the thermal characterisation was performed jointly on both thermal boundary conditions. Additional simulations at intermediate porosity (φ = 0.45, 0.65) and Reynolds-number values (≈ 45, ≈ 85) were performed exclusively for validation purposes and were not included in the regression procedure.

3. Hydrodynamic characterisation

3.1. Friction coefficient and friction factor

Fig. 4 reports the normalised velocity field within the Gyroid unit cell for two representative Reynolds numbers. The Gyroid, when aligned with the flow direction along one of its principal axes, benefits from the presence of "through-holes", as shown in Savoldi et al. (2025), Gajetti et al. (2025) for detailed morphological analysis. At $Re = 20$, the flow remains smooth and spatially distributed, with velocity variations primarily dictated by the local cross-sectional area of the passages. Increasing the Reynolds number to $Re = 100$ produces stronger local accelerations and a more heterogeneous velocity distribution, reflecting the increasing role of inertial effects. Nevertheless, the flow remains fully laminar and no large-scale flow separation is observed.

Fig. 5 reports the friction coefficient C_f and the friction factor f as a function of Reynolds number for all porosities, independent of the heat transfer and thermal boundary conditions. Both quantities decrease monotonically with Re, with higher porosities exhibiting lower friction levels.

3.2. Verification of the analytical $f(\varphi, Re)$ correlation

From regression of the CFD dataset (Gajetti, 2026), the following porosity-dependent correlations are obtained:

$$D_{h,rel}(\varphi) = 4\,\frac{\varphi}{-5.723\,\varphi^2 + 5.729\,\varphi + 1.665}, \tag{34}$$

$$K_{rel}(\varphi) = 0.0157\,\varphi^{2.72}. \tag{35}$$

$$C_F(\varphi) = 0.0784\,\varphi^{-2.04}, \tag{36}$$

Fig. 6 compares the CFD friction factor with its analytical fit obtained by substituting Eq. (34), Eq. (35) and Eq. (36) into Eq. (23). The ratio $f_{\mathrm{CFD}}/f_{\mathrm{corr}}$ remains very close to unity across the entire domain of porosity and Reynolds number, typically within ±15%. The absence of any deviation from this trend at the highest values of Re confirms that the proposed correlation remains valid throughout the investigated Reynolds-number range. Moreover, the validation points shown in Fig. 6, corresponding to Reynolds numbers (Re = 45 and Re = 85) and porosity values (φ = 0.45 and φ = 0.65) not included in the regression dataset, are also accurately predicted by f_{corr}, further confirming the robustness and predictive capability of the proposed correlation beyond the fitting domain.

Table 1
Predictive performance of the proposed hydraulic correlation.

Metric	Regression ($N = 45$)	Validation ($N = 4$)
MAPE (%)	5.81	6.09
RMSE (%)	6.85	6.91
Mean bias (%)	0.47	−2.17
Maximum relative error (%)	18.52	8.46

Table 1 provides a quantitative assessment of the correlation accuracy for both the regression and validation datasets. The proposed correlation exhibits a mean absolute percentage error (MAPE) of approximately 6% and a root mean square error (RMSE) below 7% for both datasets, while the mean bias remains below ±2.5%. The comparable error levels obtained for the validation points indicate that the correlation retains good predictive capability for operating conditions not included in the fitting procedure and does not exhibit significant overfitting.

In addition to the comparison already presented in Gajetti et al. (2025), a further assessment against independent literature data is reported in Fig. 7. This comparison provides an additional evaluation of the proposed hydraulic correlation over the Reynolds-number range relevant to the present study. Since different definitions of Reynolds number and friction factor are adopted in the literature, all datasets were first recast using the pore velocity and Darcy friction factor, consistently with the definitions employed in the present work. For $\varphi \simeq 0.35$, the experimental measurements of Hirokawa and Miyata (2024) exhibit the same decreasing trend with Re_{D_h} predicted by the present correlation, although systematically larger friction-factor values are obtained. Such differences are not unexpected, since their

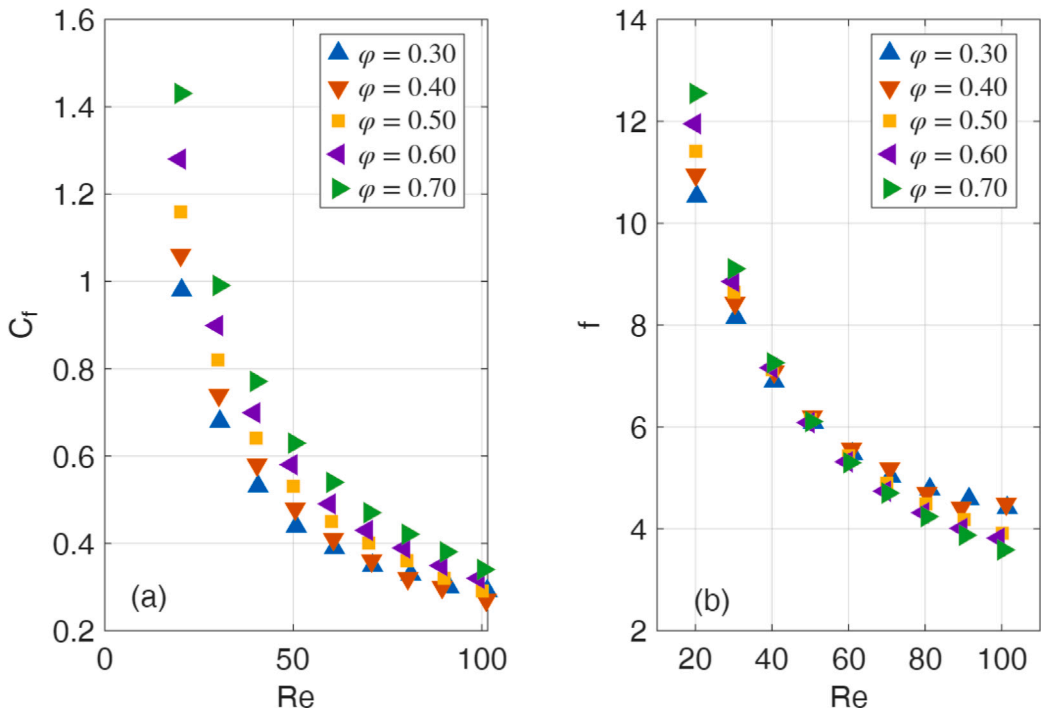

Fig. 5. Hydrodynamic behaviour of the Gyroid: (a) $C_f(Re)$; (b) $f(Re)$. Symbols represent CFD data for different porosities, solid markers for T_{wall} data.

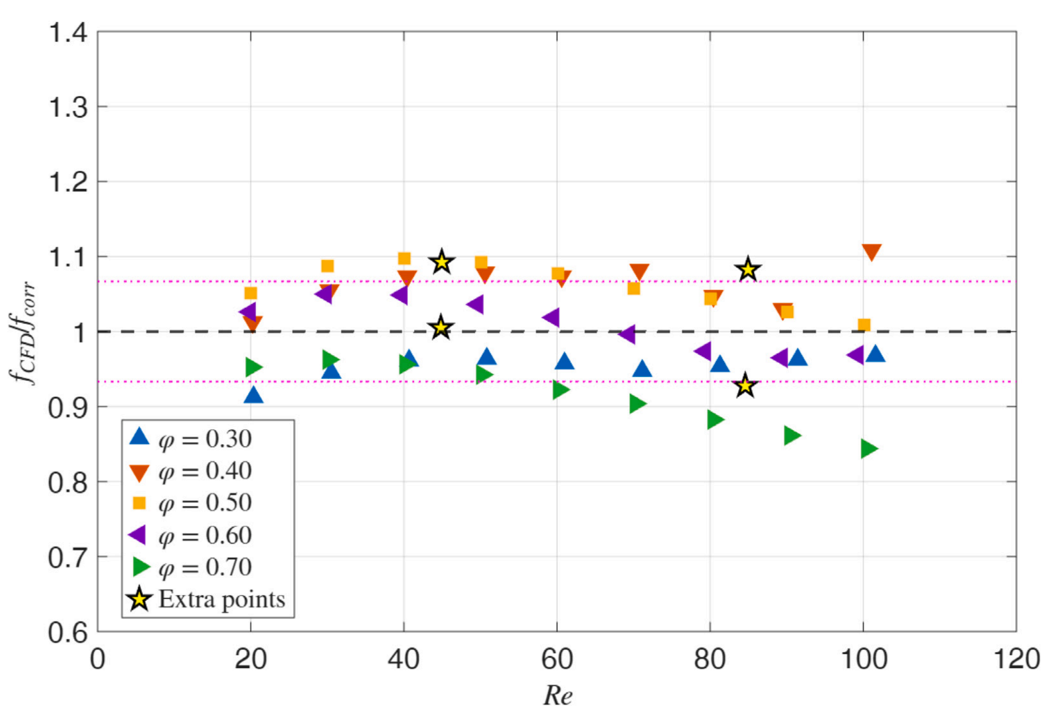

Fig. 6. Numerical verification of the analytical friction-factor correlation $f(\varphi, Re)$ through the ratio $f_{\mathrm{CFD}}/f_{\mathrm{corr}}$. Points not belonging to the database used for the correlation development are also highlighted.

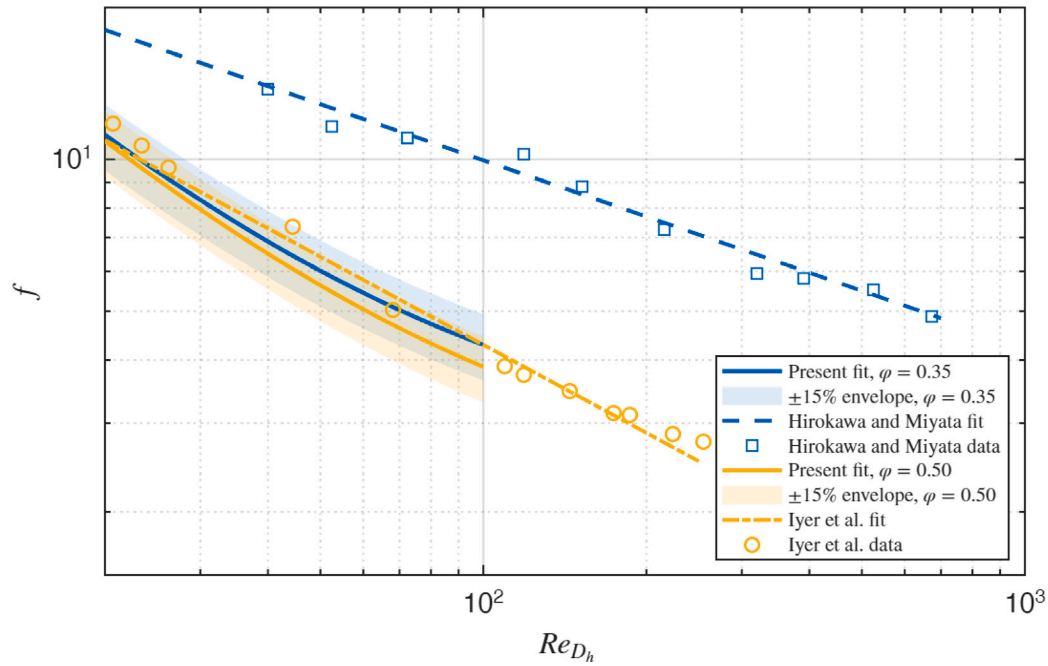

Fig. 7. Comparison of the present Darcy friction-factor correlations with independent literature results for Gyroid structures. The present correlations for $\varphi = 0.35$ and $\varphi = 0.50$ are shown with their $\pm 15\%$ envelopes and compared with the experimental measurements of Hirokawa and Miyata (2024) and the numerical results of Iyer et al. (2022), respectively. All literature data and correlations are expressed using the Darcy friction factor and the pore-velocity-based Reynolds number adopted in the present work.

measurements were performed on additively manufactured SUS316L specimens and therefore include finite-size effects, manufacturing imperfections and surface roughness (reported up to $Ra = 7.7\,\mu\text{m}$), which are absent from the ideal periodic geometries considered in the present CFD simulations.

Conversely, the numerical results of Iyer et al. (2022), corresponding to $\varphi = 0.50$, show excellent agreement with the proposed correlation throughout the common Reynolds-number range. Since their simulations, similarly to the present work, assume hydraulically smooth surfaces, the reported data remain close to, and largely within, the $\pm 15\%$ envelope of the present correlation. The experimental results of Reynolds et al. (2023) were also examined but are not included in Fig. 7. Once their Reynolds number and friction factor are converted to the definitions adopted here, most of their data fall outside the interval $20 \leq Re_{D_h} \leq 100$ investigated in the present work. More importantly, Reynolds et al. (2023) themselves observed an unexpected dependence of the friction factor on hydraulic diameter and explicitly suggested that the conventional hydraulic-diameter definition may not fully capture the hydrodynamic behaviour of TPMS structures. This observation is consistent with the subsequent analysis of Corrêa et al. (2026), who highlighted significant discrepancies among the available Gyroid friction-factor datasets and questioned the ability of conventional channel-based metrics to provide a universal hydraulic characterisation. Taken together, these comparisons further support the Darcy–Forchheimer framework adopted in the present work while simultaneously highlighting the need for dedicated experimental validation under geometrically and dynamically matched conditions, as also discussed in Savoldi et al. (2026).

As the analytical expression developed here accurately captures both the viscous and form-drag contributions to the pressure losses in the Gyroid, it provides a robust hydraulic basis for the subsequent Reynolds-analogy correlations and the thermo–hydraulic optimisation study.

3.3. Interpretation through Darcy–Forchheimer parameters

While the hydraulic behaviour discussed so far has been expressed in terms of the conventional Reynolds number and friction factor, the Darcy–Forchheimer framework introduced in Section 2.4 provides an alternative interpretation of the flow physics. In particular, the permeability-based Reynolds number Re_K and the Forchheimer number Fh allow the relative importance of viscous and inertial effects to be quantified independently of the hydraulic-diameter scaling.

Fig. 8 reports the evolution of the Forchheimer number throughout the investigated parameter space. At the lower end of the investigated Reynolds-number range, all configurations exhibit $Fh < 1$, indicating that pressure losses are primarily governed by viscous effects. As the Reynolds number increases, Fh grows approximately linearly and approaches unity, particularly for the lower-porosity configurations. For $\varphi = 0.3$, $\varphi = 0.4$ and $\varphi = 0.5$, values exceeding $Fh = 1$ are reached near the upper limit of the investigated range, indicating that inertial losses become comparable to or larger than the viscous contribution.

The increase of Fh with decreasing porosity reflects the combined effect of lower permeability and larger inertial coefficients in denser structures. Consequently, low-porosity Gyroids enter the mixed Darcy–Forchheimer regime at significantly lower Reynolds numbers Re_{D_h} than highly porous configurations. These results show that the investigated interval $20 \leq Re \leq 100$ does not merely correspond to a generic laminar regime, but spans a physically relevant transition from predominantly Darcian transport to a mixed viscous–inertial regime. This transition will be shown in the following sections to have a direct impact on the thermal behaviour and on the form of the modified Reynolds analogy. Note that the transition occurs while the flow remains fully laminar, demonstrating that significant inertial effects may develop in TPMS structures even in the absence of turbulence.

4. Thermal characterisation

The normalised temperature fields corresponding to the velocity maps in Fig. 4 are shown in Fig. 9. The evolution qualitatively mirrors the behaviour previously observed in the velocity field (Fig. 4). The increasing similarity between the thermal and hydrodynamic distributions suggests that momentum and heat transfer mechanisms evolve in a coupled manner, providing additional support for the Reynolds-analogy framework investigated in the following sections.

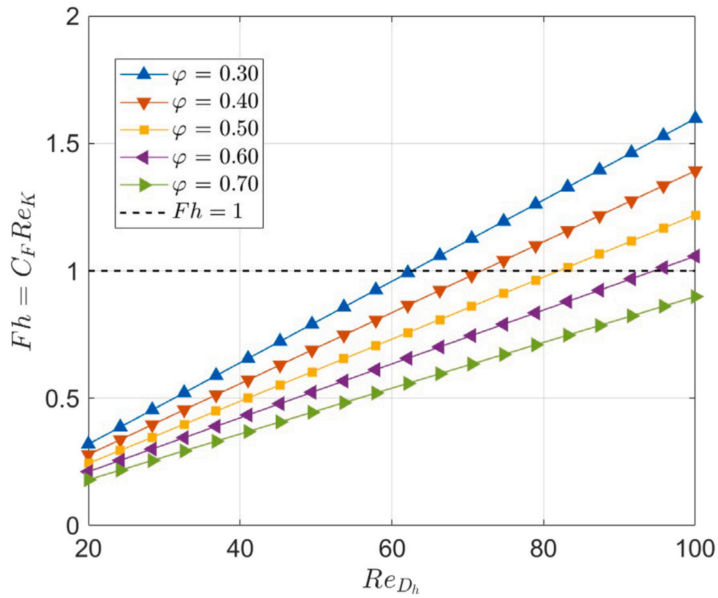

Fig. 8. Evolution of the Forchheimer number $Fh = C_F Re_K$ as a function of the hydraulic-diameter-based Reynolds number for the investigated porosity range. The dashed line indicates $Fh = 1$, corresponding to equal viscous and inertial contributions in the Darcy–Forchheimer equation.

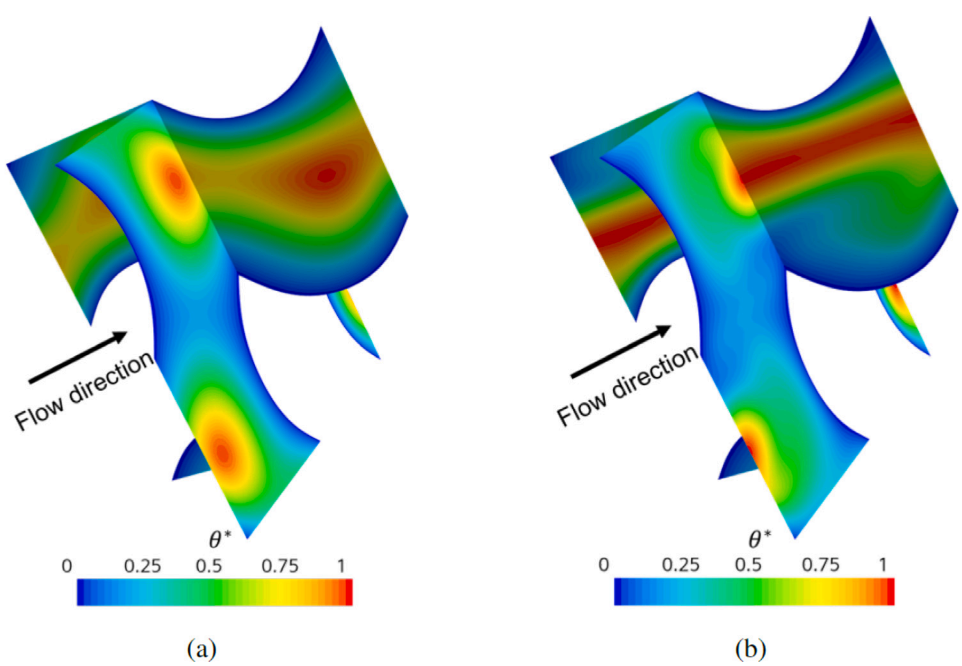

Fig. 9. Distribution of the reduced temperature θ at $Re = 20$ (a) and $Re = 100$ (b).

4.1. Nusselt number

The evolution of $Nu(Re_{D_h})$ under the two thermal boundary conditions is shown in Fig. 10. The prescribed wall temperature case leads to similar Nusselt numbers to those computed with the imposed heat-flux at the wall. In both cases, Nu tends to increase with Re_{D_h}, reflecting the growing contribution of convective transport. Note that the dependence on Re is for all cases sublinear. Beyond the Reynolds-number dependence shown in Fig. 10, Fig. 11 reveals that the influence of porosity changes qualitatively across the investigated range of Re_{D_h}. At low Reynolds numbers (Re_{D_h} = 20–40), Nu varies monotonically with φ. In this viscosity-dominated regime, convective enhancement is weak and heat transfer is largely controlled by diffusion across relatively thick thermal boundary layers. The Nusselt number therefore scales primarily with the geometric length scale, represented by the hydraulic diameter D_h, which increases with porosity.

At higher Reynolds numbers ($Re_{D_h} \approx 80-100$), inertia introduces a competing mechanism. Low-porosity configurations generate higher pore velocities, enhancing the heat-transfer coefficient, but are associated with smaller hydraulic diameters. High-porosity geometries, conversely, benefit from larger D_h but exhibit weaker convective intensification. The resulting balance between dynamic and geometric contributions leads to the non-monotonic $Nu(\varphi)$ behaviour observed in Fig. 11.

The non-monotonic trend at $Re = 100$ is in strong qualitative agreement with the correlations reported in Cheng et al. (2021) for air with $Pr \approx 0.7$, a value comparable to the present unit Prandtl number assumption. This consistency across similar Pr regimes strengthens the

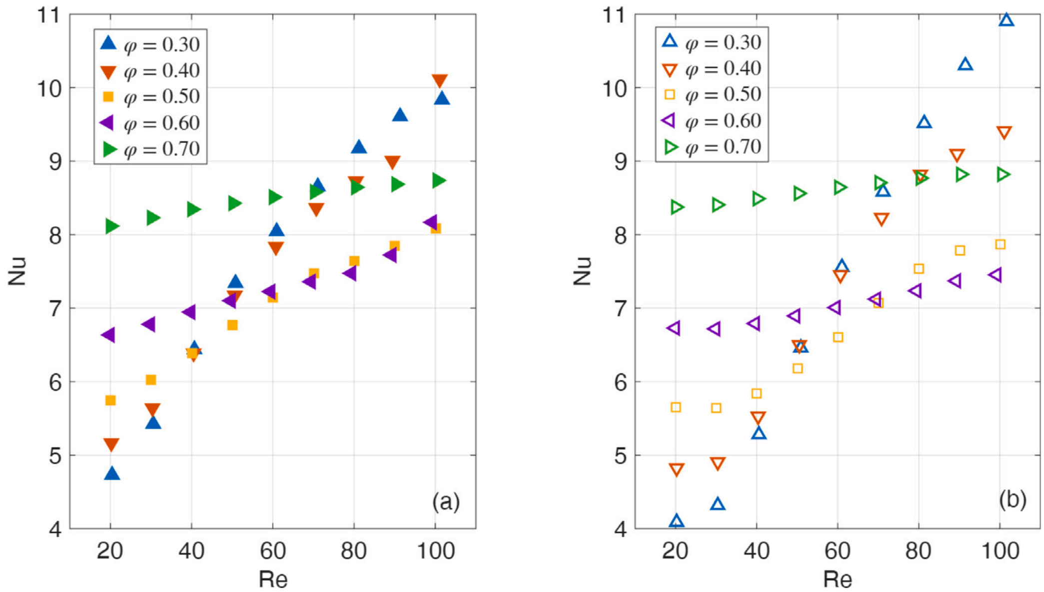

Fig. 10. $Nu(Re)$ for the Gyroid with (a) prescribed wall temperature and (b) imposed heat flux.

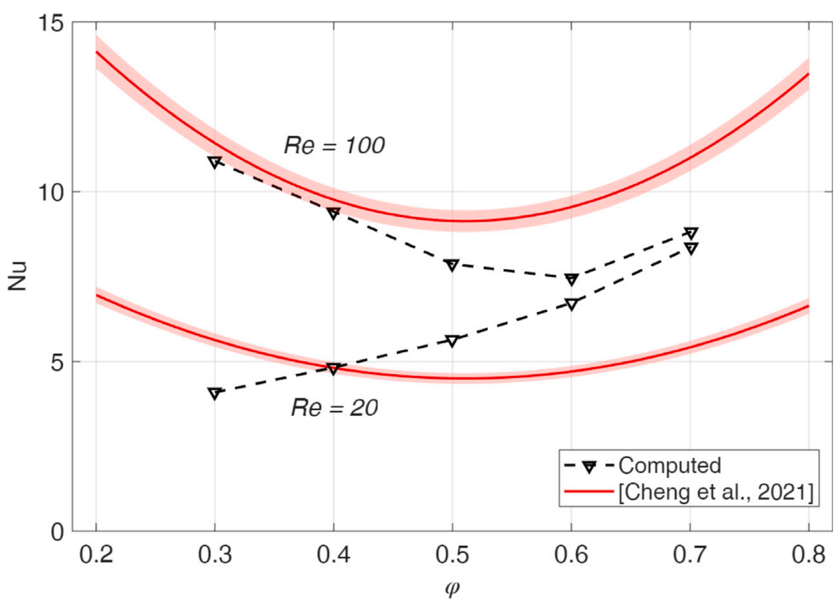

Fig. 11. $Nu(\varphi)$ for the Gyroid at Re = 20 and Re = 100, as computed in the present study for constant heat flux at the wall, compared to the fit in Cheng et al. (2021).

credibility of the computed trends. Minor quantitative deviations can reasonably be attributed to the averaging procedure adopted in Cheng et al. (2021), which includes entrance effects over multiple cells in series and is known to increase the mean Nusselt number. Other studies such as Wang et al. (2023), Zhang et al. (2025) or Dube Kerme et al. (2024) are not directly comparable to the results in this study as the range of Reynolds number or porosity does not overlap with the ranges investigated here.

The interpretation provided above is also consistent with the Darcy–Forchheimer analysis presented in Section 3.3. At low Reynolds numbers, all investigated configurations exhibit $Fh < 1$, indicating that viscous transport mechanisms dominate the flow field. In this regime, the influence of porosity on the Nusselt number is primarily geometric, through its effect on the hydraulic diameter. As Re_{D_h} increases and Fh approaches unity, inertial effects become progressively more important, introducing the competing mechanisms responsible for the non-monotonic behaviour observed at $Re = 100$.

4.2. Interpretation using permeability-scaled quantities

The previous discussion was conducted using the conventional hydraulic-diameter-based quantities Re_{D_h} and Nu, consistently with the majority of the TPMS heat-transfer literature. However, the Darcy–Forchheimer framework introduced in Section 2.4 suggests that an alternative interpretation can be obtained using permeability-scaled quantities.

In particular, the permeability-based Nusselt number (Eq. (29)) provides a measure of the heat-transfer performance based on the characteristic length scale naturally associated with transport in porous media. Fig. 12 reports the evolution of Nu_K as a function of the Forchheimer number Fh. Although the present Reynolds-analogy correlations are not formulated in terms of Nu_K, several trends observed previously become easier to interpret when expressed using permeability-scaled quantities. For all porosities, Nu_K increases monotonically with

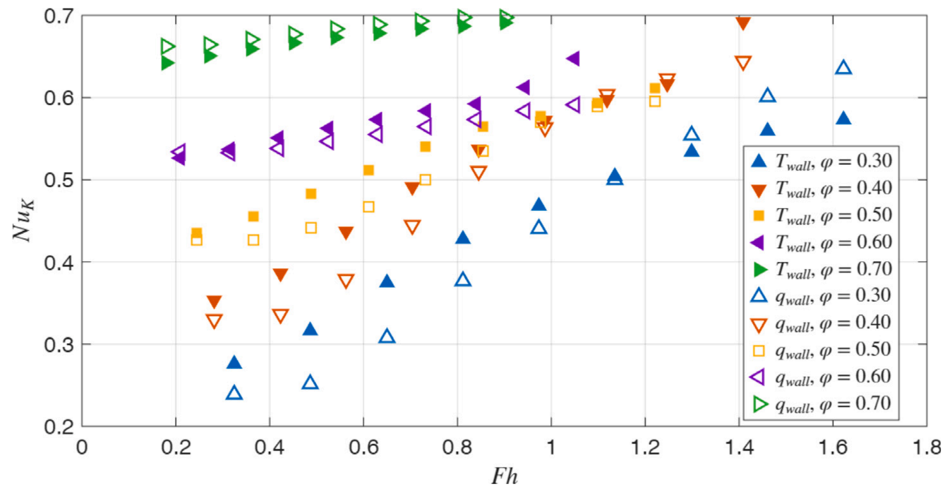

Fig. 12. Permeability-scaled Nusselt number Nu_K as a function of the Forchheimer number Fh for the investigated porosity range. Filled symbols correspond to the constant wall temperature boundary condition (T_w), whereas open symbols refer to the constant wall heat-flux condition (q_w).

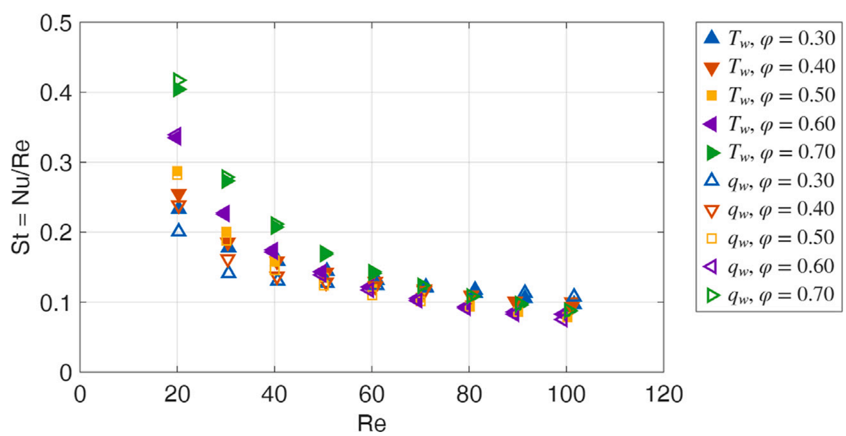

Fig. 13. Stanton number $St(Re)$ for T_{wall} (filled markers) and q_{wall} (open markers).

Fh, confirming the growing influence of inertial transport mechanisms. However, the absence of a complete collapse over a single line demonstrates that the thermal behaviour cannot be described by the Forchheimer number alone and remains strongly influenced by the geometric characteristics of the Gyroid, represented here by the porosity.

This interpretation is fully consistent with the discussion presented in Section 4.1: at low Reynolds numbers, where $Fh < 1$ for all investigated porosities, the Nusselt number is primarily controlled by geometric factors and exhibits a monotonic dependence on porosity. At higher Reynolds numbers, where several configurations approach or exceed $Fh = 1$, inertial contributions become significant and the competition between geometric and dynamic effects gives rise to the non-monotonic behaviour shown in Fig. 11.

4.3. Stanton number and Reynolds analogy trends

Fig. 13 shows the Stanton number as a function of Reynolds number for the two thermal boundary conditions. Since the Nusselt number increases sublinearly with Reynolds number, the Stanton number decreases monotonically throughout the investigated range, exhibiting a trend qualitatively similar to that of the friction factor. The close agreement between T_w and q_w datasets further confirms that the thermal boundary condition has only a minor influence on the global thermo–hydraulic behaviour of the Gyroid in laminar conditions (unlike what is typically observed in conventional channels or pipes). The similar dependence of St and f on Reynolds number provides the first indication that a reduced-order relationship linking thermal and hydraulic performance may exist. This observation motivates the development of the modified Reynolds analogies presented in the following section.

5. Gyroid Reynolds-analogy correlations

Following the philosophy of classical and modified Reynolds analogies, the Stanton number is therefore expressed as a function of porosity, Reynolds number and friction factor. The objective is not to derive a universal Reynolds analogy, but rather to identify compact engineering correlations capable of reproducing the coupled thermo–hydraulic behaviour of the Gyroid over the investigated parameter range.

Three candidate forms of modified Reynolds analogy were tested for the Gyroid. Each takes the generic structure:

$$St = a\,\varphi^{n}\,Re^{m(\varphi)}\,f.$$

where the correlation coefficients are determined by transforming the power-law expressions into a linear form through logarithms and solving the resulting overdetermined system by ordinary least squares regression.

For each candidate correlation, the CFD data were normalised in order to explicitly determine the parameter a. A successful correlation is therefore characterised by the collapse of the normalised data around

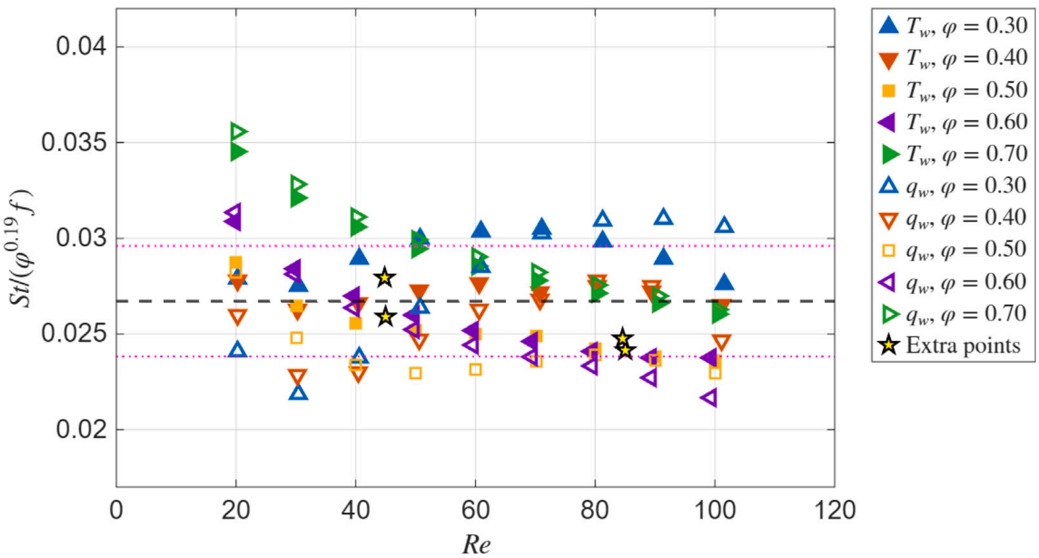

Fig. 14. Normalised Stanton number $St/(\varphi^{0.19} f)$ as a function of Re. The values collapse around 0.0267 with a standard deviation of ±11% (red dotted line). The validation points are represented with stars.

the constant value a, with limited residual dependence on Reynolds number, porosity or thermal boundary condition.

5.1. Correlation 1 (minimal)

This is the simplest of the three models and requires only φ and f as inputs, making it attractive for experimental applications:

$$St = 0.0267\,\varphi^{0.19} f \tag{37}$$

Fig. 14 shows that the normalised data collapse around the constant value 0.0267 with a scatter (standard deviation) of approximately ±11%. Considering that no explicit Reynolds-number dependence is included in the correlation, this result indicates that the friction factor alone captures a substantial fraction of the thermo–hydraulic coupling within the investigated parameter range.

Nevertheless, a residual dependence on Reynolds number remains visible in Fig. 14, particularly for the highest porosity values. Moreover, the validation points corresponding to intermediate porosities ($\varphi = 0.45$ and $\varphi = 0.65$) and Reynolds numbers ($Re = 45$ and $Re = 85$), which were not included in the regression procedure, exhibit an increasing deviation as Reynolds number increases. These observations suggest that, although the friction factor contains most of the relevant hydraulic information, an additional Reynolds-number correction is required to accurately reproduce the progressive evolution of the thermo–hydraulic behaviour over the investigated operating range.

Despite its simplicity, Correlation 1 provides a useful first-order estimate of the heat-transfer performance when only hydraulic measurements are available.

5.2. Correlation 2 (Re_{D_h} dependent)

Fig. 15 shows the normalised Stanton number obtained using the second correlation form, where both the porosity exponent and the Reynolds-number exponent are determined through regression of the CFD dataset. The resulting correlation is

$$St = 0.135\varphi^{2.06} Re_{D_h}^{0.440-\varphi} f. \tag{38}$$

The normalised values remain clustered around a constant level, with a standard deviation of approximately 15%. Although slightly larger than those obtained for Correlations 1 and 3, the residuals are distributed much more symmetrically about the fitted value. Moreover, the validation points, corresponding to intermediate porosities and Reynolds numbers not included in the regression procedure, are located on both sides of the correlation, indicating a good interpolation capability and the absence of significant systematic bias. A notable feature of the correlation is the porosity-dependent Reynolds exponent,

$$m(\varphi) = 0.440 - \varphi. \tag{39}$$

For low porosities the exponent remains positive, whereas it progressively decreases with increasing porosity and eventually becomes negative. This behaviour reflects the progressively weaker influence of Reynolds number on the Stanton number as the porosity increases, consistently with the thermo–hydraulic trends discussed in Sections 3 and 4. Unlike Correlations 1 and 3, the second formulation therefore introduces a porosity-dependent Reynolds-number correction, which is shown in Section 6 to play a key role in reproducing the observed thermo–hydraulic trade-offs and the resulting Pareto front.

5.3. Correlation 3 (weakly Re_{D_h} dependent)

A third correlation was investigated in an attempt to reduce the explicit Reynolds-number dependence while reducing its sensitivity to porosity. The resulting expression is

$$St = 0.034\varphi^{0.20} Re^{-0.061-0.0023\varphi} f. \tag{40}$$

Fig. 16 shows that the correlation provides a satisfactory collapse of the CFD database, with a normalised standard deviation of approximately 12%, comparable to that obtained for Correlation 1. The very small coefficient multiplying the porosity-dependent Reynolds exponent (−0.0023) indicates that the Reynolds-number dependence is almost independent of porosity.

Although Correlation 3 exhibits a slightly smaller normalised scatter than Correlation 2, a closer inspection reveals systematic deficiencies that are not captured by the standard deviation alone. In particular, the low- and high-porosity datasets ($\varphi = 0.3$ and 0.7) show a clear systematic deviation from the fitted value, while the validation points remain predominantly on the same side of the correlation. These observations indicate that the reduced scatter is partly achieved at the expense of introducing a residual bias.

Correlation 3 therefore represents an intermediate formulation between Correlations 1 and 2. Unlike Correlation 1, it formally retains an explicit Reynolds-number dependence. However, the almost vanishing porosity-dependent Reynolds correction makes its behaviour very

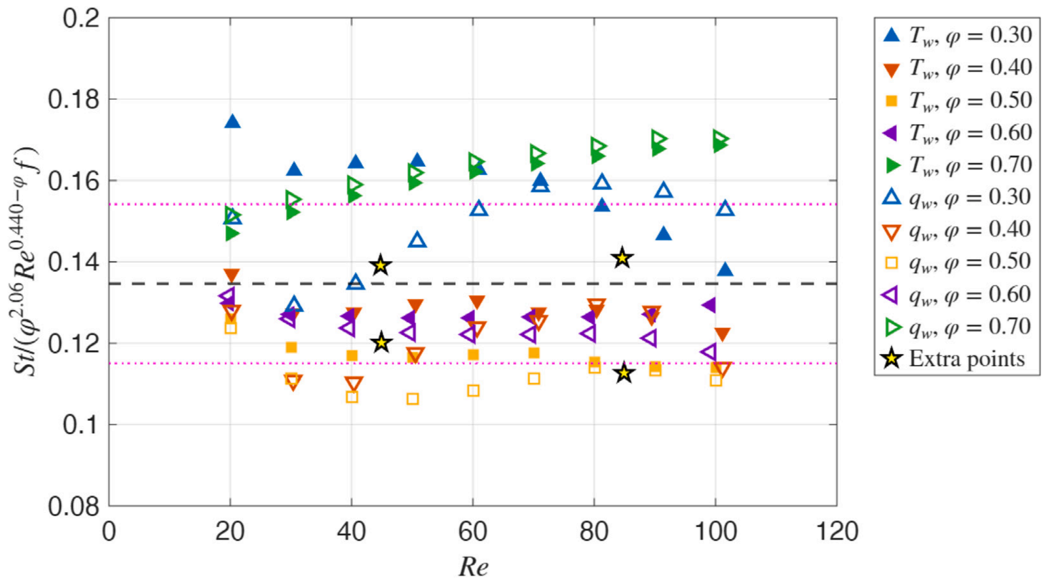

Fig. 15. Normalised Stanton number $St/(\varphi^{2.06}Re^{0.440-\varphi}f)$. The values collapse around 0.134 with a standard deviation of ±15% (red dotted line). The validation points are represented with stars.

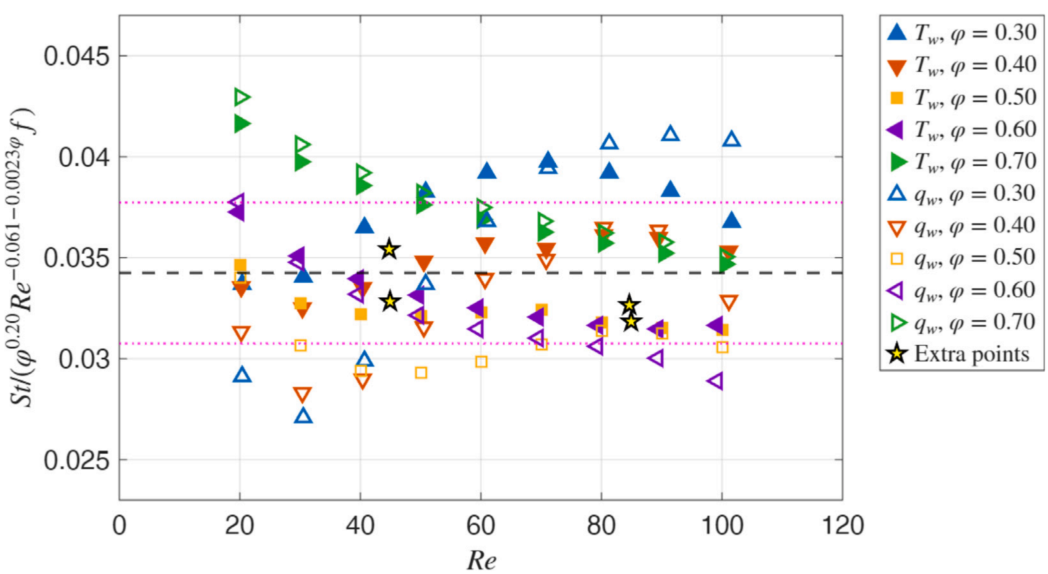

Fig. 16. Normalised Stanton number $St/(\varphi^{0.20}Re^{-0.061-0.0023\varphi}f)$. The values collapse around 0.0342 with a standard deviation of ±12% (red dotted line), similarly to the first correlation. The validation points are represented with stars.

similar to that of the minimal correlation. The comparison among the three formulations therefore suggests that the slightly larger normalised standard deviation of Correlation 2 should not be interpreted as a deterioration of the fit. Rather, it reflects the introduction of a physically meaningful Reynolds-number correction, which removes the systematic residual bias and improves the interpolation capability across the investigated parameter space.

6. Multi-objective optimisation: heat transfer vs pumping power

The Reynolds-analogy correlations developed in the previous section enable a reduced-order thermo–hydraulic optimisation of the Gyroid. Once the hydraulic behaviour is known, the proposed framework allows the thermal response to be reconstructed without performing additional thermal CFD simulations, representing one of the main practical advantages of the present methodology. The optimisation is formulated as the following bi-objective problem in the (φ, Re) design space:

$$\max(Nu), \qquad \min(P_{pump})$$

The optimisation is intentionally expressed in terms of the conventional quantities Nu and P_{pump}, consistently with the Reynolds-number-based framework adopted throughout this work. Although alternative porous-medium representations based on Nu_K, Re_K, Fh and P_K can also be defined, they are employed solely as interpretative tools and do not affect the optimisation procedure. Since the Pareto fronts are constructed from the dimensionless quantities Nu and $\varphi f Re^3/D^4_{h,\mathrm{rel}}$, they represent intrinsic thermo–hydraulic trade-offs between heat-transfer enhancement, hydraulic resistance and inertial transport, independently of specific operating conditions or dimensional constraints. Consequently, the resulting Pareto-optimal configurations should be regarded as design guidelines rather than unique optima, since the final choice of (φ, Re) will ultimately depend on additional constraints such as allowable pressure drop, manufacturing limitations or thermal-load requirements.

6.1. Pareto fronts for the three fits

Figs. 17–19 show the Pareto-optimal sets obtained using the three Reynolds-analogy correlations. Each curve represents the non-dominated configurations for which no other (φ, Re) pair yields simultaneously a higher Nu and a lower P_{pump}. The Pareto fronts were obtained by exhaustively evaluating the analytical correlations over a uniform grid spanning the entire calibrated design space, using 121 equally spaced values of porosity ($0.3 \leq \varphi \leq 0.7$) and Reynolds number ($20 \leq Re \leq 100$), corresponding to a total of 14 641 candidate configurations. No interpolation or extrapolation outside the fitted domain was performed. Pareto-optimal solutions were identified through an exhaustive non-dominated sorting procedure: a configuration was classified as dominated if another configuration exhibited both a lower hydraulic-cost index and an equal or higher Nusselt number, with at least one of the two objectives being strictly improved. The uncertainty associated with the fitted correlations was not propagated to the Pareto fronts; consequently, the optimisation results should be interpreted as deterministic predictions based on the best-fit correlations.

The absence of a unique optimal Reynolds number in Fig. 17 can be understood by expressing the friction-factor correlation of Eq. (23) as the sum of a viscous contribution, $A(\varphi)$, multiplied by Re^{-1}, and an inertial contribution, $B(\varphi)$:

$$A(\varphi) = 2\varphi \frac{D_{h,\mathrm{rel}}^2}{K_{\mathrm{rel}}}, \qquad B(\varphi) = 2\varphi^2 \frac{D_{h,\mathrm{rel}} C_F}{\sqrt{K_{\mathrm{rel}}}}. \tag{41}$$

For Correlation 1, $St = C_1 \phi^{0.19} f$, and therefore the corresponding Nu:

$$Nu = St Re = C_1 \varphi^{0.19} f Re \tag{42}$$

Substituting Eq. (23) into Eq. (42) yields

$$Nu = C_1 \varphi^{0.19} \left[A(\varphi) + B(\varphi) Re\right]. \tag{43}$$

The hydraulic-cost index can be written as

$$P_{\mathrm{pump}} \propto \frac{\varphi}{D_{h,\mathrm{rel}}^4} \left[A(\varphi) Re^2 + B(\varphi) Re^3\right]. \tag{44}$$

Thus, at fixed porosity, increasing Re simultaneously increases both heat-transfer performance and hydraulic cost. A higher-Re point cannot dominate a lower-Re point because it provides a larger Nu at the price of a larger P_{pump}, while a lower-Re point has the opposite behaviour.

Consequently, the Pareto front collapses onto the upper porosity boundary ($\varphi \approx 0.7$), while spanning the entire investigated Reynolds-number range. No intermediate porosity provides a better thermo–hydraulic compromise within the investigated domain.

In contrast, Correlation 2 (Fig. 18) generates an internal Pareto front, indicating the existence of genuine thermo–hydraulic trade-offs within the investigated design space. Unlike Correlations 1 and 3, the Pareto-optimal solutions of which collapse onto the upper porosity boundary, Correlation 2 predicts that both porosity and Reynolds number become independent design variables. This behaviour can be understood by considering the analytical form of the second Reynolds analogy (Eq. (38)), which, after introducing the Darcy–Forchheimer decomposition, becomes

$$Nu = C_2 \varphi^{2.06} \left[A(\varphi) Re^{0.44-\phi} + B(\varphi) Re^{1.44-\phi}\right]. \tag{45}$$

Unlike Correlation 1, the Reynolds-number dependence is explicitly modulated by porosity through the exponents $(0.44 - \varphi)$ and $(1.44 - \varphi)$. As porosity increases, both exponents decrease, progressively reducing the thermal benefit associated with increasing Reynolds number. The optimisation therefore balances the competing effects of permeability, inertial losses and convective heat transfer, giving rise to the internal Pareto front observed in Fig. 18. Consequently, neither porosity nor Reynolds number alone is sufficient to identify the optimal thermo–hydraulic configuration. The emergence of an internal Pareto front only for Correlation 2 further supports the physical relevance of the porosity-dependent Reynolds-number correction introduced in the second Reynolds analogy.

For Correlation 3 (Fig. 19), the Pareto front again collapses onto the upper porosity boundary, similarly to Correlation 1. Although the third Reynolds analogy formally retains an explicit Reynolds-number dependence, the fitted coefficient multiplying the porosity-dependent Reynolds correction is almost zero. Consequently, the Reynolds-number dependence becomes nearly independent of porosity, and the optimisation reverts to a boundary-dominated solution in which the highest porosity remains systematically Pareto-optimal throughout the investigated design space. The comparison between the three Pareto fronts therefore highlights the importance of the porosity-dependent Reynolds correction. Only Correlation 2, for which the Reynolds exponent varies significantly with porosity, is capable of reproducing the coupled thermo–hydraulic trade-offs that give rise to an internal Pareto front.

7. Conclusions

This work has developed and numerically verified a modified Reynolds analogy for the Gyroid TPMS in the laminar regime, extending the preliminary concepts introduced in Savoldi et al. (2025). The investigated operating window was expanded to porosities up to $\varphi = 0.7$ in the range $20 \leq Re \leq 100$, and complemented by explicit hydraulic correlations for $f(\varphi, Re)$ and three alternative Reynolds-analogy formulations relating Stanton number and friction factor.

The analysis showed that the investigated Reynolds-number range spans a physically relevant transition from a predominantly Darcian regime to a mixed Darcy–Forchheimer regime while remaining entirely laminar. The introduction of the permeability-based quantities Re_K and Fh provides a physical interpretation of this transition and of the corresponding evolution of the thermo–hydraulic behaviour.

The proposed framework enables the prediction of the thermal performance of infinite solid Gyroid lattices in laminar, non-conjugate heat transfer directly from hydraulic information, without performing dedicated thermal simulations. Once the friction factor and porosity are known, the proposed correlations allow the direct estimation of the Stanton and Nusselt numbers. The proposed hydraulic correlation also shows good agreement with independent numerical data available in the literature, while comparison with experimental measurements confirms the same overall hydraulic trends.

Among the three candidate formulations, Correlation 2 (Eq. (38)) provides the most physically consistent representation of the thermo–hydraulic coupling. Although its normalised standard deviation is slightly larger than those of the other two formulations, it eliminates the systematic residual bias, provides a more robust interpolation of the validation points, and is the only correlation capable of reproducing the internal Pareto front observed in the thermo–hydraulic optimisation. This result indicates that introducing a porosity-dependent Reynolds-number correction is essential to capture the coupled influence of geometry and inertial transport on the thermal performance of the Gyroid. More generally, the present work demonstrates that Reynolds-analogy concepts can be reformulated within a porous-medium framework to provide reduced-order thermo–hydraulic models for architected lattice structures.

The proposed analogy is presently limited to incompressible flows with $Pr = 1$ and to the investigated ranges of Reynolds number and porosity. Although developed here for the Gyroid topology, the proposed methodology can in principle be extended to other TPMS architectures once the corresponding hydraulic transport properties have been characterised. Future work should therefore assess this generalisation, together with the extension to non-unity Prandtl numbers and transitional or turbulent flow regimes, and provide dedicated experimental validation on additively manufactured Gyroid structures.

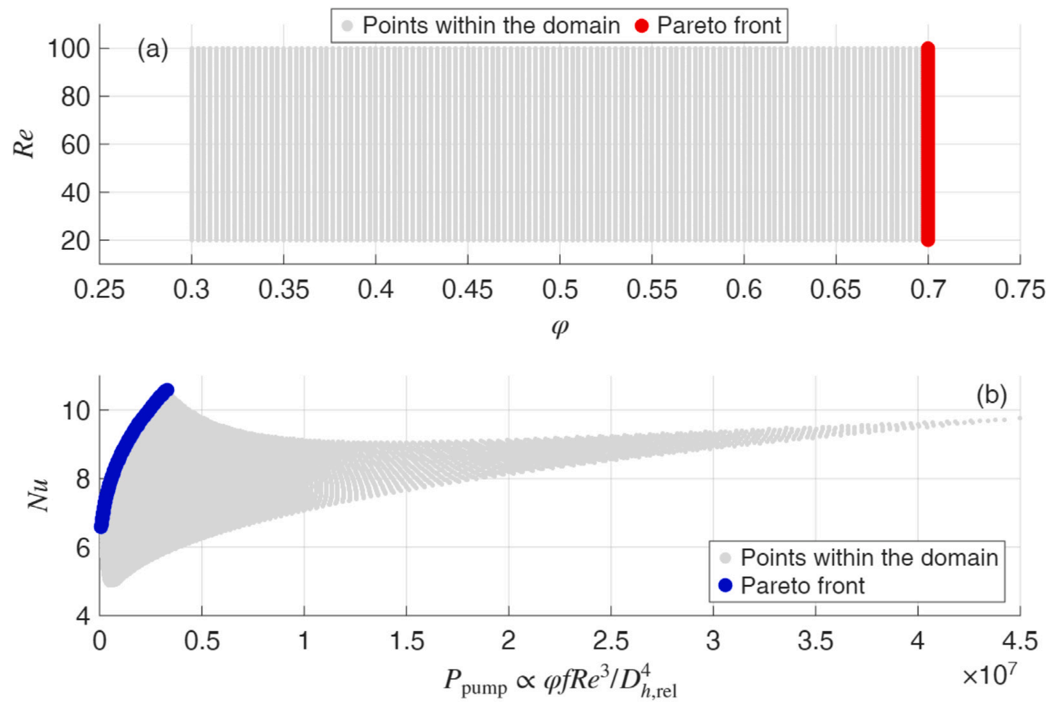

Fig. 17. Boundary-dominated Pareto fronts in the (Re, φ) plane (a) and (Nu, P_{pump}) plane (b), obtained using Correlation 1.

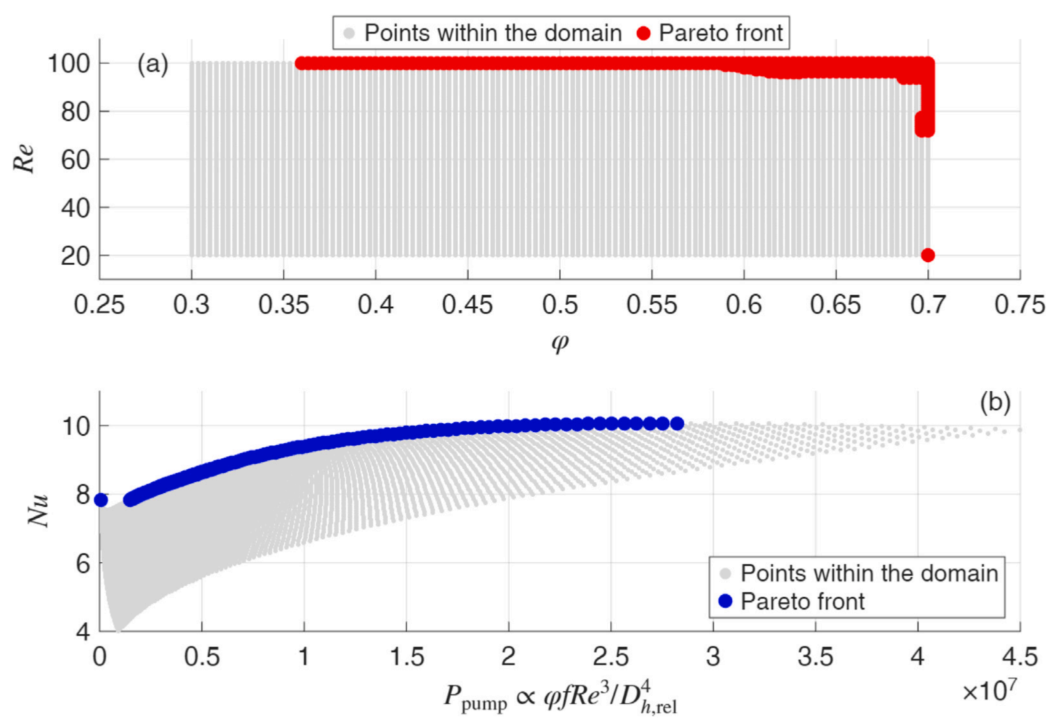

Fig. 18. Internal Pareto fronts in the (Re, φ) plane (a) and (Nu, P_{pump}) plane (b), obtained using Correlation 2.

CRediT authorship contribution statement

L. Savoldi: Writing – original draft, Visualization, Validation, Supervision, Software, Resources, Project administration, Methodology, Investigation, Funding acquisition, Formal analysis, Conceptualization. **A. Cammi:** Writing – review & editing, Methodology, Investigation, Formal analysis, Conceptualization. **E. Gajetti:** Visualization, Software, Formal analysis, Data curation. **L. Marocco:** Writing – review & editing, Methodology, Formal analysis, Conceptualization.

Declaration of Generative AI usage

During the preparation of this work, the authors used ChatGPT to improve the manuscript readability. The authors reviewed and edited

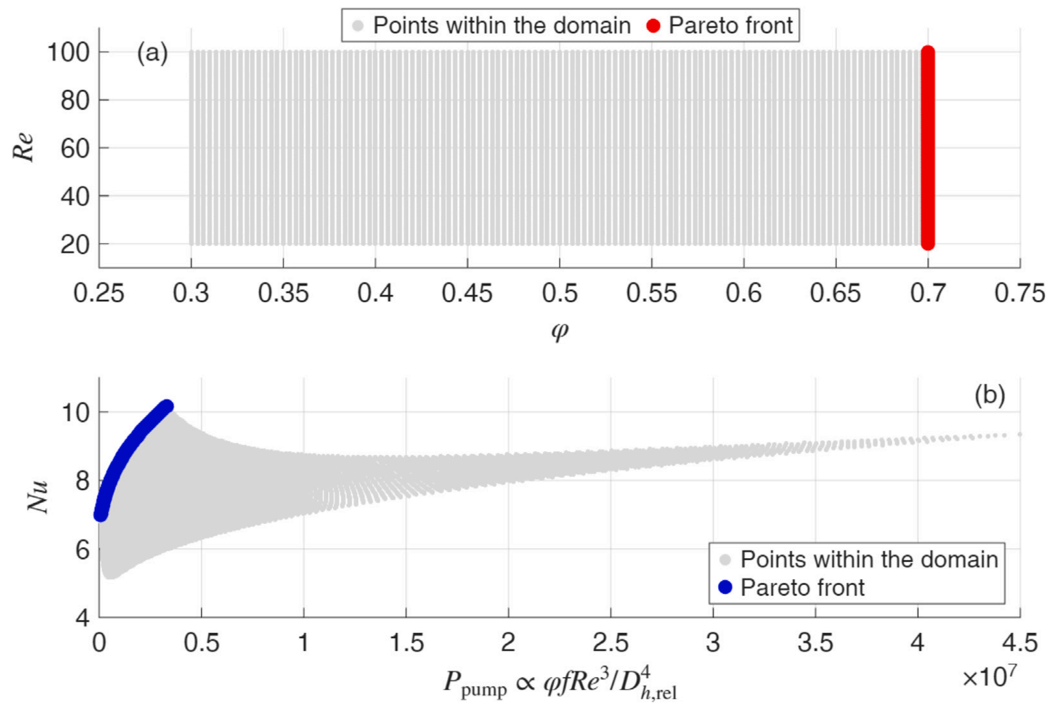

Fig. 19. Boundary-dominated Pareto fronts in the (Re, φ) plane (a) and (Nu, P_{pump}) plane (b), obtained using Correlation 3.

the content and take full responsibility for the content of the published article.

Declaration of competing interest

The authors declare that they have no known competing financial interests or personal relationships that could have appeared to influence the work reported in this paper.

Acknowledgements

The authors gratefully acknowledge the feedback from Mr. F. Bruno and Dr. W. Ferretto.

Data availability

Data will be made available on request.

References

American Society of Mechanical Engineers (ASME), 2009. Standard for Verification and Validation in Computational Fluid Dynamics and Heat Transfer, ASME V&V 20–2009. American Society of Mechanical Engineers, New York, NY, USA.

Bergman, T.L., Lavine, A.S., Incropera, F.P., DeWitt, D.P., 2011. Introduction To Heat Transfer, sixth ed. Wiley.

Brambati, G., Guilizzoni, M., Foletti, S., 2024. Convective heat-transfer correlations for TPMS-based heat exchangers. Appl. Therm. Eng. 242, 122492.

Carpenter, A., Jin, F., 2024. Pore-scale multi-objective shape optimisation of TPMS lattices. Int. J. Heat Mass Transfer 223, 124948.

Cengel, Y.A., Ghajar, A.J., 2014. Heat and Mass Transfer: Fundamentals and Applications. McGraw-Hill.

Cheng, Z., Li, X., Xu, R., Jiang, P., 2021. Investigations on porous media customized by triply periodic minimal surface: Heat transfer correlations and strength performance. Int. Commun. Heat Mass Transfer 129, 105713.

Chilton, T.H., Colburn, A.P., 1934. Mass transfer (absorption) coefficients: prediction from heat-transfer and fluid-friction data. Ind. Eng. Chem. 26, 1183–1187.

Corrêa, C.E.B., Martins, G.S.M., Zilio, G., Jaskowiak, P.A., Paiva, K.V., 2026. Pressure drop prediction in gyroid triply periodic minimal surfaces structures using experimental data, computational fluid dynamics and artificial neural networks. Appl. Therm. Eng. 285, 129238.

Dube Kerme, E., Hajialibabei, M., Ziad Saghir, M., El-Ketan, O., 2024. Experimental investigation of porous gyroid structure: Effect of cell size and porosity on performance. Therm. Sci. Eng. Prog. 53, 102728.

Dutkowski, K., Kruzel, M., Rokosz, K., 2022. Review of the state-of-the-art uses of minimal surfaces in heat transfer. Energies 15, 7994.

ESI OpenCFD, 2026. OpenFOAM® v2212. https://www.openfoam.com/news/main-news/openfoam-v2212. (Accessed: Feb 2026).

Forooghi, P., Stroh, B., et al., 2021. Turbulent flow over rough surfaces: a review. Int. J. Heat Fluid Flow 89, 108774.

Fukagata, K., Iwamoto, K., Kasagi, N., 2002. Contribution of Reynolds stress distribution to the skin friction in wall-bounded flows. Phys. Fluids 14 (11), L73–L76.

Gado, M.G., Al-Ketan, O., Aziz, M., Abu Al-Rub, R.K., 2024. Triply periodic minimal surface structures: Design, fabrication, 3D printing techniques, state-of-the-art studies, and prospective thermal applications for efficient energy utilization. Energy Technol. 12 (5), 2301287.

Gajetti, E., 2026. Triply Periodic Minimal Surfaces As Structured Porous Media Cooling Systems for the Removal of High Heat Fluxes (Ph.D. thesis). Politecnico di Torino.

Gajetti, E., Boccardo, G., Savoldi, L., Marocco, L., 2025. Hydrodynamic characterisation of gyroid, diamond and split-p tpms structures as porous media. J. Heat Mass Transf. 252, 127439.

Hirokawa, T., Miyata, H., 2024. Experimental investigation on pressure drop characteristics of adiabatic two-phase flow in a gyroid-structured channel. Int. J. Multiph. Flow 181, 104982.

Incropera, F.P., DeWitt, D.P., Bergman, T.L., Lavine, A.S., 2011. Fundamentals of Heat and Mass Transfer, seventh ed. Wiley.

Iyer, J., Moore, T., Nguyen, D., Roy, P., Stolaroff, J., 2022. Heat transfer and pressure drop characteristics of heat exchangers based on triply periodic minimal and periodic nodal surfaces. Appl. Therm. Eng. 209, 118192.

Khalil, M., Hassan Ali, M.I., Khan, K.A., Abu Al-Rub, R., 2022. Forced convection heat transfer in heat sinks with topologies based on triply periodic minimal surfaces. Case Stud. Therm. Eng. 38, 102313.

Mahulikar, S.P., Herwig, H., 2008. Fluid friction in incompressible laminar convection: Reynolds analogy revisited for variable fluid properties. Eur. Phys. J. B 62, 77–86.

Men, Z., Chen, W., Li, Q., Liu, S., 2025. Topology optimization of the IWP triply periodic minimal surfaces (TPMS) heat sink based on porous media effective model. Int. J. Heat Mass Transfer 240, 126657.

nTop, 2026. Guide to lattice structures in additive manufacturing. https://www.ntop.com/resources/blog/guide-to-lattice-structures-in-additive-manufacturing/. (Accessed: Feb 2026).

Padrão, D., Hancock, D., Paterson, J., Tuck, C., Maskery, I., 2024. New structure–performance relationships for surface-based lattice heat sinks. Appl. Therm. Eng. 236, 121572.

Park, D.H., Moon, J.Y., Chung, B.J., 2024. Reynolds analogy in a packed bed for a high Prandtl number fluid. Int. J. Heat Mass Transfer 232, 125917.

Reynolds, B.W., Fee, C.J., Morison, K.R., Holland, D.J., 2023. Characterisation of heat transfer within 3D printed TPMS heat exchangers. Int. J. Heat Mass Transfer 212, 124264.

Samson, S., Tran, P., Marzocca, P., 2023. Design and modelling of porous gyroid heatsinks: Influences of cell size, porosity and material variation. Appl. Therm. Eng. 235, 121296.

Savoldi, L., Gajetti, E., Cammi, A., Marocco, L., 2025. Investigating the Reynolds analogy for TPMS in laminar regime. Proc. THMT-25. Tokyo.

Savoldi, L., et al., 2026. Use of triply periodic minimal surface lattices for heat transfer applications: A systematic literature investigation. Energies 19 (3).

Saxena, A., Ansari, D., Hosain, L., Duwig, C., 2025. A novel gyroid-based two-inlet heat sink for enhancing heat dissipation and mitigating hot spots in power electronics cooling. Energy Convers. Manag.: X 27, 101076.

Secchi, F., Gatti, D., Piomelli, U., Frohnapfel, B., 2025. A framework for assessing the Reynolds analogy in turbulent forced convection over rough walls. J. Fluid Mech. 1006, R3.

Sucec, S., 2020. Rough-surface turbulent boundary-layer heat transfer using generalized Reynolds analogies. J. Heat Transf. 142, 101801.

Wang, J., Chen, K., Zeng, M., Ma, T., Wang, Q., Cheng, Z., 2023. Investigation on flow and heat transfer in various channels based on triply periodic minimal surfaces (TPMS). Energy Convers. Manag. 283, 116955.

Wu, X., Hibiki, T., 2025. Analogy between pressure-drop coefficient and nusselt number for packed-bed channels. Int. Commun. Heat Mass Transfer 162, 108651.

Yan, G., Liu, Y., Zhang, Z., Sun, M., Li, S., Zhang, X., Jiang, L., Xing, S., Mao, Y., 2024. Thermal-hydraulic performance of modified Schwarz–diamond solid-network triply periodic minimal surface structures. Appl. Therm. Eng. 249, 123384.

Yeranee, K., Rao, Y., 2022. A review of recent investigations on flow and heat transfer enhancement in cooling channels embedded with TPMS. Energies 15, 8994.

Zhang, Y., Bi, W.-T., She, Z.-S., 2014. A generalized Reynolds analogy for compressible wall-bounded turbulent flows. J. Fluid Mech. 739, 392–420.

Zhang, Y., Huang, H., Liu, R., Kong, H., Qian, L., Xu, X., Zhang, Z., 2025. Research on the flow and heat transfer performance of solid-network triply periodic minimal surface structures. Int. Commun. Heat Mass Transfer 167 (A), 109323.